Coordination Chemistry Reviews 253 (2009) 2261–2285

Contents lists available at ScienceDirect

Coordination Chemistry Reviews

journal homepage: www.elsevier.com/locate/ccr

Review

Tetranuclear complexes in molecular magnetism: Targeted synthesis, high-field EPR and pulsed-field magnetization

Phalguni Chaudhuri[a,*], Vladislav Kataev[b,**], Bernd Büchner[b], Hans-Henning Klauss[c], Berthold Kersting[d,***], Franc Meyer[e,****]

[a] Max-Planck-Institut für Bioanorganische Chemie, Stiftstrasse 34-36, 45470 Mülheim an der Ruhr, Germany
[b] Institute for Solid State Physics, IFW Dresden, Helmholtzstrasse 20, D-01069 Dresden, Germany
[c] Institute for Solid State Physics, Technische Universität Dresden, D-01062 Dresden, Germany
[d] Institut für Anorganische Chemie, Universität Leipzig, Johannisallee 29, D-04103 Leipzig, Germany
[e] Institut für Anorganische Chemie, Georg-August-Universität, Tammannstraße 4, D-37077 Göttingen, Germany

Contents

* Corresponding author. Fax: +49 208 306 3951.
** Corresponding author. Fax: +49 351 4659 414.
*** Corresponding author. Fax: +49 341 973 6199.
**** Corresponding author. Tel.: +49 551 393012; fax: +49 551 393063.
E-mail addresses: chaudhuri@mpi-muelheim.mpg.de (P. Chaudhuri), V.Kataev@ifw-dresden.de (V. Kataev), b.kersting@uni-leipzig.de (B. Kersting), franc.meyer@chemie.uni-goettingen.de (F. Meyer).

0010-8545/$ – see front matter © 2009 Elsevier B.V. All rights reserved.
doi:10.1016/j.ccr.2009.03.024

ARTICLE INFO

Article history:
Received 31 October 2008
Accepted 26 March 2009
Available online 5 April 2009

Keywords:
Magnetic properties
Oligonuclear complexes
EPR spectroscopy
Metalloligands
Thiolate ligands
Bridging ligands
Pyrazolate ligands
Azide ligands

ABSTRACT

The present article reviews the synthetic approaches, the structures and the spectroscopic and magnetic properties of three different types of tetranuclear complexes: systems with metal/oximate metalloligands, tetranuclear complexes based on polydentate amine-thiophenolate ligands, and nickel/azido complexes with compartmental pyrazolate scaffolds. In all three cases, well-defined bimetallic entities have been used as building blocks for the controlled synthesis of higher-nuclearity systems. This has allowed one to modulate the magnetic properties of the tetrametallic cores and to specifically target low-spin or high-spin ground states. High-frequency high-field EPR and pulsed-field magnetization measurements have been used to experimentally determine spin Hamiltonian parameters and to probe the magnetic responses at high fields.

© 2009 Elsevier B.V. All rights reserved.

1. Introduction

The German Research Council (Deutsche Forschungsgemeinschaft) initiated a few years ago a priority program called "Molecular Magnetism" encompassing physicists and chemists not only from Germany but also from other countries in the European Community. One of the objectives of the program was to bring together scientists from different fields, but with a common interest at magnetism of molecular species. The projects funded for six years (2002–2008) by the German Research Council were successfully completed, as illustrated here through the final reports on a variety of tetranuclear complexes by the authors. This article hopefully illustrates the value of looking at synthesis (preparative chemistry) from a molecular magnetism perspective, a lesson that obviously extends well beyond tetranuclear complexes. This review on tetranuclear complexes is expected to demonstrate also successful collaborations between different groups of chemists and physicists.

At present, the field of molecular magnetism [1] is addressing the synthesis and study of discrete polynuclear complexes in an attempt to improve our understanding of the mechanism involved in exchange coupling and the production of new paramagnetic clusters with high-spin and strong anisotropy (super-paramagnetic molecules). Exchange-coupled polymetallic complexes, in which spin coupling between paramagnetic metal ions is propagated via bridging atoms, are of special interest to researchers who seek new molecule-based magnetic materials [2]. Current emphasis lies on the targeted preparation of polynuclear transition–metal complexes with a large number of unpaired electrons in their spin ground state. This is mainly due to the fact that such compounds may behave as single-molecule magnets (SMMs) [3], that is, they can display hysteresis effects similar to those of bulk magnets but of molecular origin [4,5]. SMMs thus offer a molecular approach to magnetic materials, and their potential applications include information storage at the molecular level [6–8] and use as quantum bits in quantum computation [9–11].

Most molecule-based magnets are composed of several paramagnetic transition–metal ions, in which the metal ions are bridged via carboxylate, alkoxide, oxide, azide and cyanide bridges [12]. Many strategies have been employed over the last 25 years to obtain molecule-based magnets [13]. The use of mononuclear metal complexes of macrocyclic ligands with active coordination sites for cross-linking by suitable bridging ligands has also proven to be a very powerful strategy for the well-defined arrangement of paramagnetic transition metal ions [14–16]. Only a few groups, however, have considered higher-nuclearity complexes as building blocks for the preparation of molecule-based magnets [17,18].

It is a general phenomenon that despite the interest in the properties of exchange-coupled polymetallic systems, synthetic methods have yet to reach the level of efficiency attained with mononuclear complexes. The present contribution summarizes the results for new synthetic approaches, where well-defined binuclear complexes have been used as building blocks to assemble in a controlled fashion larger systems of higher nuclearity.

Following this general introduction related to molecular magnetism, this review article comprises three self-contained subsections. They describe the three different types of systems investigated in the author's laboratories, namely tetranuclear complexes derived from metal/oximate metalloligands (Chaudhuri/Kataev), tetranuclear complexes based on polydentate amine-thiophenolate ligands (Kersting/Kataev), and tetranuclear complexes assembled from binucleating pyrazolate-based scaffolds (Meyer/Kataev/Klauss). No attempt is made to provide a comprehensive coverage of tetranuclear complexes, the focus being mainly upon results from our laboratories.

2. Tetranuclear complexes from metal/oximate metalloligands

As this is a final report of the projects funded by the German Research Council (DFG), we are refraining from citing all the papers on oximato-bridged tetranuclear complexes; we will deal here mainly with our own work.

2.1. Synthetic strategy

Among the variety of methodologies applied to synthesize polymetallic coordination compounds, the use of "metalloligands", i.e. metal complexes as ligands [19], in which the ligands already bound to one metal have a free lone pair of electrons for coordination to a second metal of the same or different kind, has proven to be very successful. We have favoured the strategy of "metal oximate" building blocks as ligands [20] to design and synthesize multinuclear heterometal complexes in a controlled fashion. A straightforward modular synthetic route involving metal-oximates has been developed and the concept of "metal complexes as ligands" is depicted for star-shaped and linear tetranuclear, both homo- and heteronuclear, complexes in modular form below (Scheme 1).

This section of the review deals specifically with a series of linear tetranuclear complexes containing tris(phenolato)dimanganese bridges and a $Cr^{III}Mn^{II}_3$-cluster that exhibits the star-shaped spin topology.

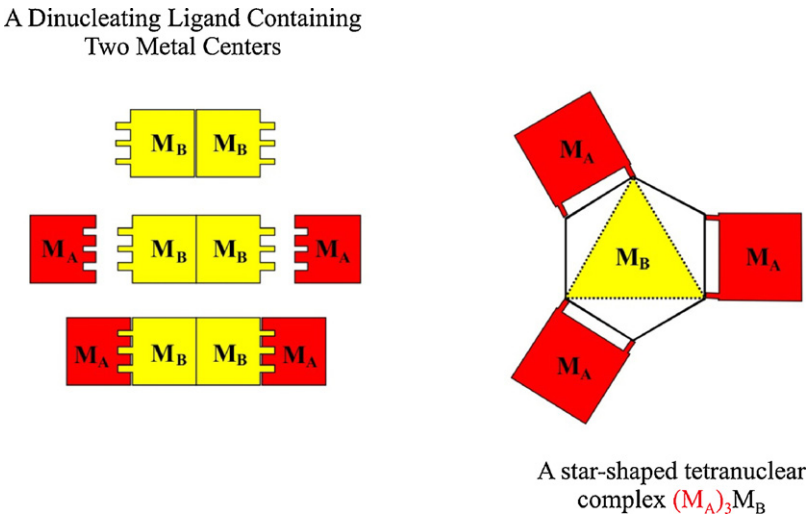

Scheme 1. Linear tetranuclear complexes $M_AM_BM_BM_A$ (left) and star-shaped tetranuclear complexes (right).

Earlier we have employed monooximates like salicylaldoxime, pyridine-2-aldoxime to isolate exchange-coupled molecules [20]. A potentially powerful but barely explored route to new polynuclear complexes is the use of dioximate ligands in place of traditional monooximate ligands. The advantages of dioximate ligands include the possibility of triggering aggregation to high-nuclearity products.

We have exploited the versatility of the dinucleating oxime, 2,6-diformyl-4-methylphenoldioxime, H_3dfmp [21], in preparing an unprecedented series of magnetochemically interesting complexes. To our knowledge no such heterometallic linear tetranuclear complexes have been reported in the literature. In our synthetic approach, a dinucleating ligand containing an oxime and an *ortho*-phenol site forms a dimanganese(II) complex by selectively complexing a divalent metal ion with octahedral coordination geometry in the free bidentate site (N_{oxime} and O_{phenol}) of the ligand, thus generating a "metal-oximate" ligand (Scheme 2, step 1) [20]. The free oxime-oxygen atoms can now bind to another metal ion, resulting in linear, tetranuclear complexes (Scheme 2, step 2) [22].

Clearly, the capping (tmtacn)M_A can be replaced by other capping reagents such as methylboronic acid $CH_3B(OH)_2$, phenylboronic acid $(C_6H_5)B(OH)_2$. Thus, we deliberately synthesized the following series [22]:

$[Et_3NH][CH_3B^{III}\{\mu\text{-}(dfmp)_3Mn^{II}{}_2\}B^{III}CH_3]$	**1**
$[Et_3NH][(C_6H_5)B^{III}\{\mu\text{-}(dfmp)_3Mn^{II}{}_2\}B^{III}(C_6H_5)]$	**1a**
$[(tmtacn)Mn^{III}\{\mu\text{-}(dfmp)_3Mn^{II}{}_2\}Mn^{III}(tmtacn)]$	**2**
$[(tmtacn)Mn^{IV}\{\mu\text{-}(dfmp)_3Mn^{II}{}_2\}Mn^{IV}(tmtacn)]$	**3**
$[(tmtacn)Cr^{III}\{\mu\text{-}(dfmp)_3Mn^{II}{}_2\}Cr^{III}(tmtacn)]$	**4**
$[(tmtacn)Fe^{III}\{\mu\text{-}(dfmp)_3Mn^{II}{}_2\}Fe^{III}(tmtacn)]$	**5**

2.2. Characterization

1 contains the identical dimetallic manganese(II) core as in **2**–**5**, but the terminal diamagnetic CH_3B^{III}-fragment in **1** has been replaced by the corresponding paramagnetic (tmtacn)M fragments, in **2**–**5** (M = Mn(III) **2**, Mn(IV) **3**, Cr(III) **4** or Fe(III) **5**).

Fig. 1 displays the structure of the monoanion in **1**. The X-ray structure confirms that a linear tetranuclear complex has indeed been formed in such a way that each manganese center with a MnN_3O_3 donor set is embedded in a clathrochelate derived from the 2,6-diformyl-4-methylphenoldioximate ligand. The central tris(oximato)dimanganese(II), $[Mn_2(dfmp)_3]^{5-}$, bridges two terminal CH_3B^{III}-centers through the deprotonated oximate oxygen atoms. All phenoxy oxygen atoms, O38, O23, and O23*, are μ_2-bridging, yielding a Mn(1)···Mn(1)* separation of 2.909(5) Å and a face-shared bioctahedral structure for the dimanganese(II) core. Such a tris(μ-phenoxo)dimanganese core is quite rare [23]. The coordination polyhedron around the manganese center is a trigonal prism with trigonal twist angles of 1.1°, 1.2° and 0°. Interestingly, in the corresponding phenylboronic acid analogue **1a**, $[C_6H_5B^{III}\{\mu\text{-}(dfmp)_3Mn^{II}{}_2\}B^{III}C_6H_5]^-$ [24], the manganese(II) centers are more distorted toward octahedron with the twist angles ranging between 7.0 and 9.8°. The Mn–O(phenoxide)–Mn angles are in the range of 86.0–86.7° for **1**, whereas the angles vary for the phenylboronic acid analogue **1a** from 84.3–85.5°. Such B-capped clathrochelates are quite common in the literature [25], particularly for the metal ions with low-spin d^6 electron configuration, but it is quite rare for high-spin Mn(II) centers [26].

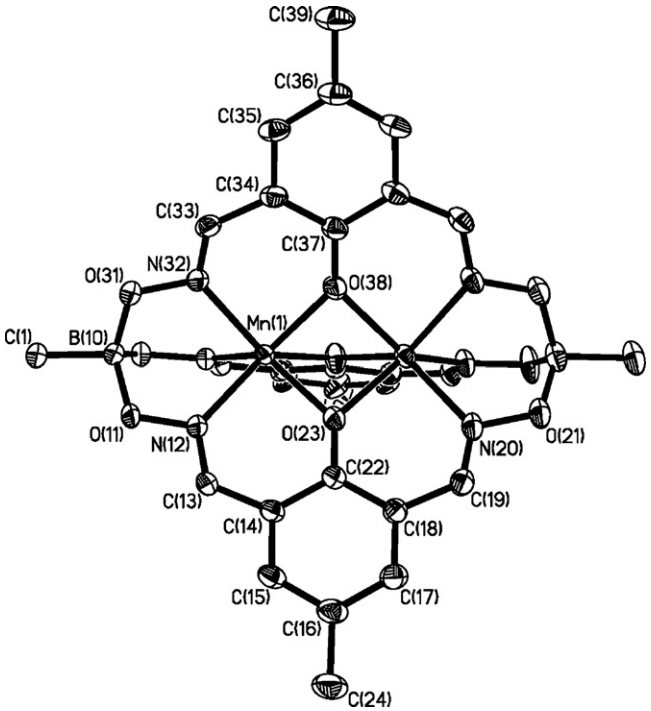

Fig. 1. ORTEP representation of the anion in complex **1**, $B^{III}Mn^{II}Mn^{II}B^{III}$. Reproduced with permission from Ref. [22].

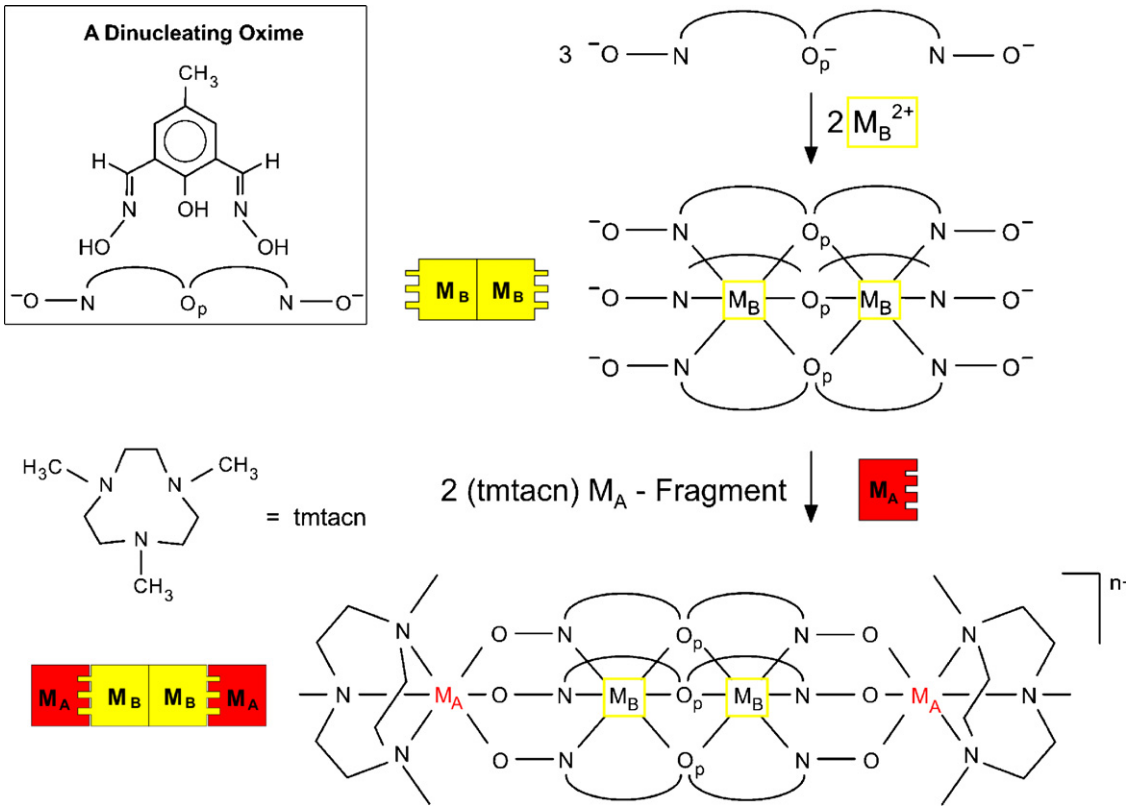

Scheme 2. Modular synthetic strategy for linear tetranuclear complexes.

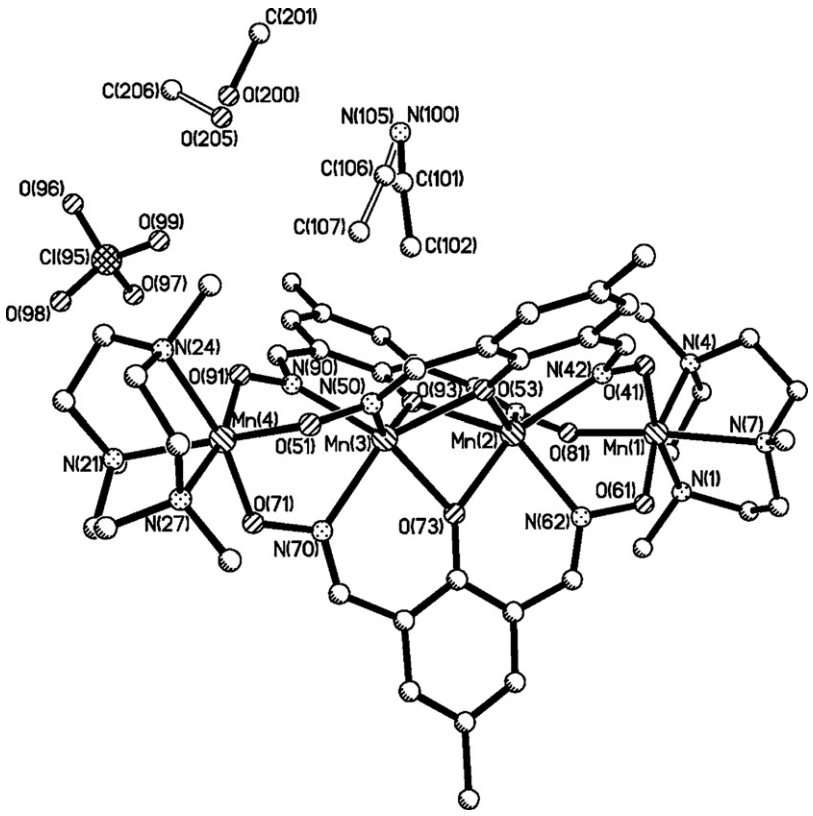

Fig. 2. Molecular structure of complex **2,** $Mn^{III}Mn^{II}Mn^{II}Mn^{III}$. Reproduced with permission from Ref. [22].

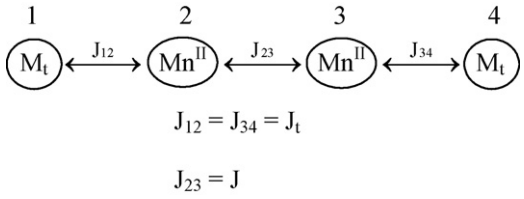

Scheme 3. Exchange coupling model used for complexes **2**–**5**.

The atom-connectivity in other complexes (**2**–**5**) is identical with N_3O_3 donor atoms for the terminal M_A metals; as an example the molecular structure of **2** is shown in Fig. 2.

Presence of Jahn-Teller distortion and other structural parameters together with the charge-balance consideration for **2** unequivocally indicate +III oxidation states for the terminal high-spin d^4 electron-configured manganese centers.

The spin-Hamiltonian in the form $\hat{H} = -2J\,\hat{S}_i \cdot \hat{S}_j$ for an isotropic exchange coupling was used to evaluate the nature and magnitude of the exchange interaction from the temperature-dependent (2–290 K) magnetic susceptibility data. As the conformations of the dimanganese(II) confacial bioctahedra for the complexes are essentially identical with one another [22] and complex **1** is magnetically only a dinuclear Mn(II) complex, we have used the intra-dimanganese(II) coupling $J = J_{23} = -9.1\ cm^{-1}$ for the least-squares fitting of the data for **2**–**5** to the model in Scheme 3.

We have used the simplest model, viz. a two-J model. The interactions between the terminal ions J_{13}, J_{24} and J_{14} were not considered, as the corresponding distances ~7 Å and 10 Å, are too long for any significant exchange interaction.

Thus, the following constraints are used for simulation [27] of the experimental magnetic data for complexes **2**–**5**: $g_{Mn(II)} = 2.00$ (fixed), $J_{23} = J = -9.1\ cm^{-1}$ (fixed); the simulated magnetic parameters are listed in Table 1.

All our attempts to use the constraint $J_{23} = J = -9.1\ cm^{-1}$ (fixed) for **3**, $Mn^{IV}Mn^{II}Mn^{II}Mn^{IV}$, failed to reproduce the observed data for **3**. Hence, both parameters J_t and J were allowed to float during the simulation and the fitting parameters, $J_t = +2.5\ cm^{-1}$, $J = -4.1\ cm^{-1}$, $g_{Mn(IV)} = 2.00$, $g_{Mn(II)} = 2.0$ for **3** were obtained, as shown also in Table 1. This unbiased fitting procedure, the details of which are given in Ref. [22], also applied for other complexes led to similar results as shown in Table 1, which clearly indicate that the terminal trivalent paramagnetic metal ions such as Cr^{III}, Mn^{III} and Fe^{III} have insignificant influence on the coupling operating between the central manganese(II) centers. On the other hand, the terminal tetravalent Mn^{IV} ions influence the intra-dimanganese(II) coupling; the parameter J for **3** is significantly weaker with $J = -4.1\ cm^{-1}$ in comparison to those for **2**, **4** and **5**. That the above exchange parameters for **3** lie well in a global minimum in the parameter space have also been checked by a three-dimensional and a two-dimensional contour projection of the relative error surface [27] for fitting the magnetic data of complex **3** as a function of both J_t and J (Fig. 3). Similarly, the global minima for other complexes were also checked.

Table 1
Magnetic parameters obtained from the data for complexes **1**–**5**.

Complex	Electron config.[a]	J_t/cm^{-1}	J/cm^{-1}	g_t[b]
1 $B^{III}Mn^{II}Mn^{II}B^{III}$	$d^0d^5d^5d^0$	–	−9.1	–
2 $Mn^{III}Mn^{II}Mn^{II}Mn^{III}$	$d^4d^5d^5d^4$	+2.4	−9.1 (fixed)	1.9
3 $Mn^{IV}Mn^{II}Mn^{II}Mn^{IV}$	$d^3d^5d^5d^3$	+2.5	−4.1 (!!)	2.00
4 $Cr^{III}Mn^{II}Mn^{II}Cr^{III}$	$d^3d^5d^5d^3$	−2.2	−9.1 (fixed)	1.90
5 $Fe^{II}Mn^{II}Mn^{II}Fe^{III}$	$d^5d^5d^5d^5$	−1.45	−9.1 (fixed)	2.00

[a] Metal centers are in high-spin configuration.
[b] $g_{Mn} = 2.00$ (fixed).

The variable-field (1, 4 and 7 T) variable-temperature (2–5 K) reduced magnetization data also led to similar results. Additionally, the axial zero-field splitting parameter D_t for the terminal metal ion Mn(III) was evaluated to be $-1.1\ cm^{-1}$ for **2**.

An important point deserving attention of this study is the result that the higher charge of terminal Mn(IV) in **3** has a profound influence on the exchange coupling prevailing in the central trisphenoxodimanganese(II) core by increasing the ferromagnetic components, arising from more covalent nature of the Mn(IV)-oxime bonds in comparison to those in **4** containing the lower-charged Cr(III), to the overall exchange. Although linear tetranuclear complexes of this type are not good candidates for generating molecules with high-spins, they are ideally suited for studying systematically influence of different parameters on the exchange coupling mechanism.

Now we describe our results of the study on the tetranuclear cluster $(M_A)_3M_B$ i.e. $Mn^{II}{}_3Cr^{III}$ (Scheme 1). We were prompted to study the ligation property of bis(pyridine-2-aldoximato)manganese(II), $Mn^{II}(PyA)_2$ unit, because of the oppor-

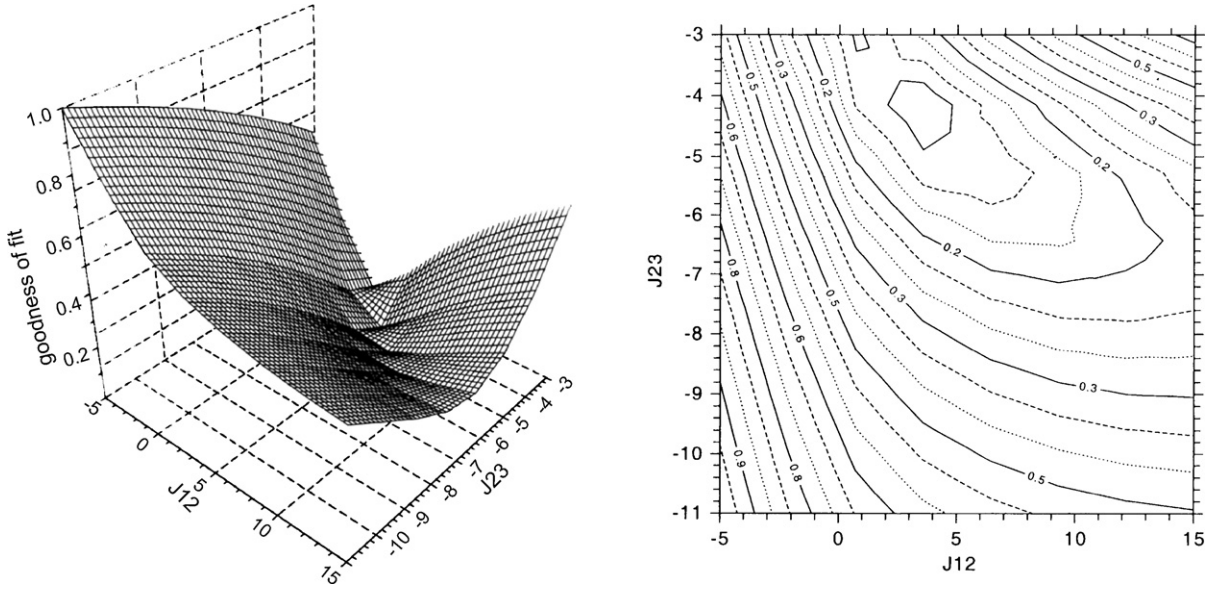

Fig. 3. A 3D- and 2D-contour projection of the relative error surface for fitting the magnetic data of complex **3**. Reproduced with permission from Ref. [22].

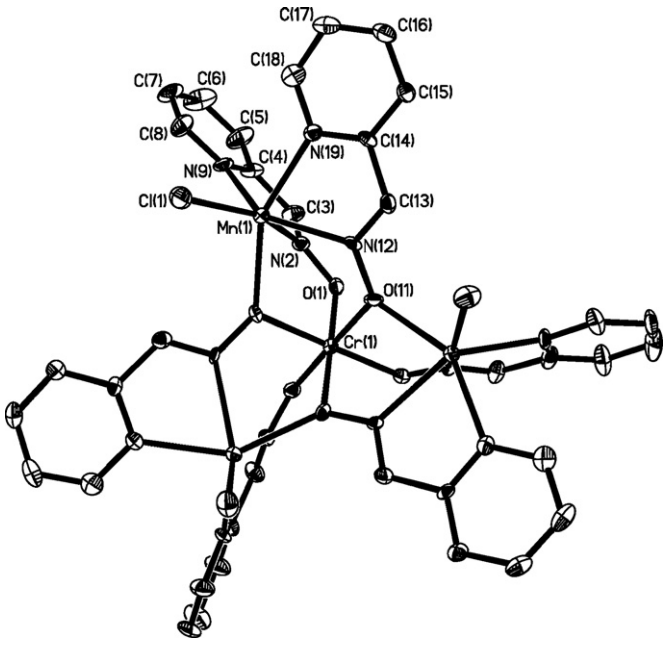

Fig. 4. A perspective view of $[Cr^{III}Mn^{II}_3(PyA)_6Cl_3]$, **6**. The percent electron density enclosed by the thermal ellipsoids is 40%, and hydrogen atoms are omitted for clarity. Reproduced by permission of The Royal Society of Chemistry [29a].

tunity for its facile *in situ* formation dictated by the thermodynamic stability of the resulting complex containing *cis* disposed two pendent oxime oxygen atoms for ligation, as is reported in the cis-disposed mononuclear $[Mn^{II}(PyAH)_2Cl_2]$ complex. [28] Our anticipation was fulfilled by isolation of the tetranuclear complex in the presence of Cr(III) ions. The star-shaped [29] heterotetranuclear complex with the *syn*-2-pyridine aldoxime (HPyA) $[Cr^{III}Mn^{II}_3(PyA)_6Cl_3]$, **6** [29a], underlines the versatility of this monooxime ligand to adopt a variety of coordination modes as described earlier in the literature [29b–e].

A perspective view of the cluster $[Cr^{III}Mn^{II}_3(PyA)_6Cl_3]$, **6**, in which PyA is the monoanion of pyridine-2-aldoxime, HPyA, is shown in Fig. 4. Complex **6** contains a $Cr^{III}Mn^{II}_3$ trigonal core with a Cr(1) atom at the center and three Mn(1) centers at the apices of an equilateral triangle with a basal edge-length of 5.49 Å. The central chromium atom Cr(1) is surrounded by an almost perfect octahedron CrO_6 of six oximato oxygen atoms, pendent from the three peripheral $Mn(PyA)_2$-fragments. The oxygen atoms are bonded to Cr(1) in two different ways as shown below.

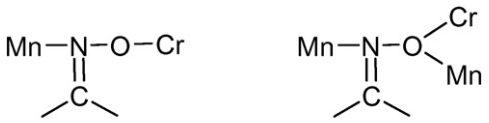

I **II**

Hence, each peripheral Mn-atom is linked to the central Cr(1) atom through one oximate (N–O) and two μ_2-O_{ox} donors. The peripheral manganese centers are six-fold coordinated yielding trigonal antiprismatic geometry with a highly distorted $MnOClN_4$ core; coordination occurs through two pyridine and two azomethine nitrogen atoms, one μ_2-oximate oxygen and a chloride ion. The metrical parameters are in accord with those for a high-spin d^5 Mn(II) and a d^3 Cr(III) ion, thus resulting in a rare example of a high-spin $Mn^{II}_3Cr^{III}$ tetranuclear star-shaped metal topology.

The magnetic susceptibility data were analyzed by using the effective spin-Hamiltonian in accord with the model (Chart 1), as

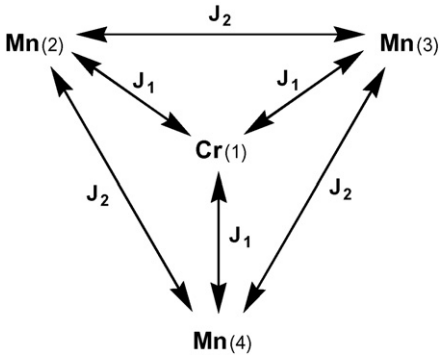

Chart 1.

shown below

$$\hat{H} = -2J_{CrMn}(\hat{S}_1 \cdot \hat{S}_2 + \hat{S}_1 \cdot \hat{S}_3 + \hat{S}_1 \cdot \hat{S}_4) - 2J_{MnMn}(\hat{S}_2 \cdot \hat{S}_3 + \hat{S}_3 \cdot \hat{S}_4 + \hat{S}_4 \cdot \hat{S}_2) + D[S_z^2 - 1/3(S(S+1))]$$

with $S_1 = 3/2$ for the central Cr(III) ion and $S_2 = S_3 = S_4 = 5/2$ for the Mn(II) ions. J_{CrMn} and $J_{MnMn} = J_2$ are the exchange parameters for the Cr(III)/Mn(II) and Mn(II)/Mn(II) interactions (Chart 1).

The simulated parameters are $J_1 = -0.40\,cm^{-1}$, $J_2 = -0.10\,cm^{-1}$, $g_{Cr} = 1.95$, $g_{Mn} = 2.00$, $D = 1.0\,cm^{-1}$. We want to stress that the quality of simulation deteriorates with $D = 0$ (fixed). Additionally, the one-J model, i.e. neglecting the J_2-path, leads to physically unreasonable results and hence the two-J model described above is preferred by us. Thus, $J_{CrMn} = J_1$ dominates over the coupling $J_{MnMn} = J_2$, resulting in frustrated Mn(II) spins.

Variable-temperature (2–290 K) variable field (1, 4 and 7 T) magnetization (VTVH) measurements were also performed and are depicted together with their simulations in Fig. 5.

The simulated parameters are $J_1 = -0.40\,cm^{-1}$, $J_2 = -0.10\,cm^{-1}$, $g_{Cr} = 1.95$, $g_{Mn} = 2.00$, $D = -1.0\,cm^{-1}$, which are identical with the parameters described earlier obtained from the susceptibility measurements at 1 T. We conclude, the paramagnetic centers in **6** are practically uncoupled and the magnetic properties at low temperatures are dominated by the zero-field splitting D of Cr(III) and Mn(II) ions resulting in closely spaced low-lying levels, which undergo splitting and crossing. High-field EPR studies have supplied additional support to the above conclusion.

A set of EPR spectra has been collected at a temperature of 10 K, in magnetic fields up to 15 T and in a frequency range between 19 and 388 GHz. The evolution of the EPR spectrum with increasing the

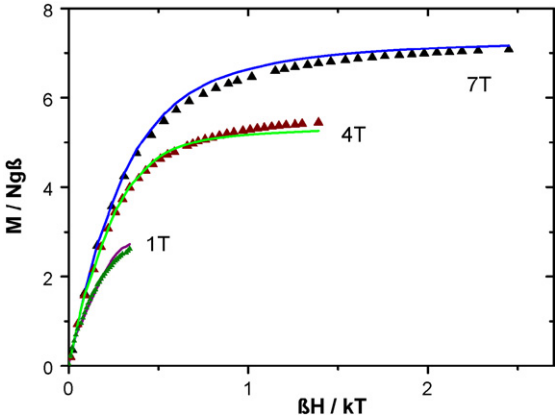

Fig. 5. Variable-temperature (2–290 K) variable-field (1, 4 and 7 T) magnetization measurements for $Cr^{III}Mn^{II}_3$. The solid lines represent the simulations with the parameters given in the text. Reproduced by permission of The Royal Society of Chemistry [29a].

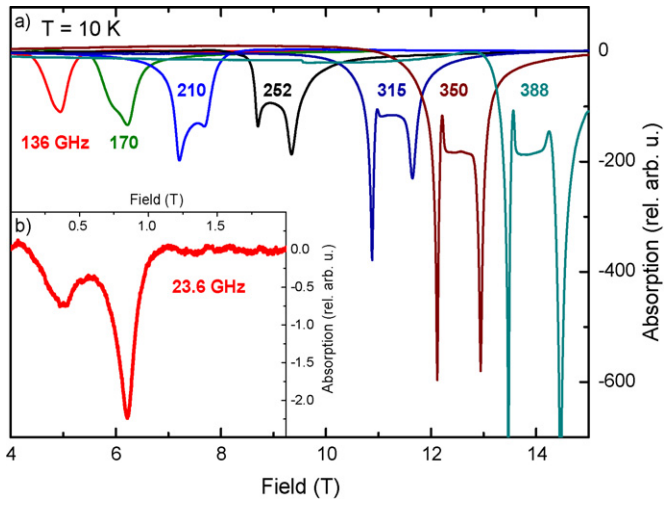

Fig. 6. Selected HF-EPR spectra measured at different excitation frequencies ν at $T = 10$ K. No signals can be seen at $\nu \leq 20$ GHz. A well-defined spectrum comprising the main peak and a weak satellite is detected first at 23.6 GHz (inset). For $\nu > 170$ GHz two sharp resonance lines on the broad dome-shaped background develop in the spectrum. Reproduced by permission of The Royal Society of Chemistry [29a].

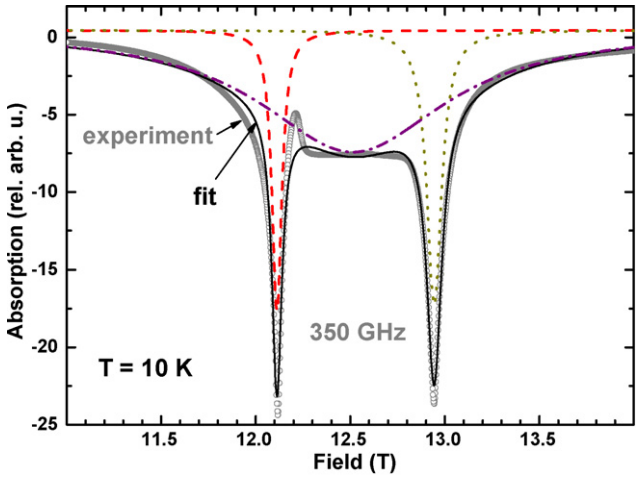

Fig. 7. Example fit of a 10 K spectrum at 350 GHz (circles) with three Lorentzian line profiles (dashed, dash-dotted and dotted line) and their sum (solid line) yielding the resulting fit (for details see the text). Reproduced by permission of The Royal Society of Chemistry [29a].

excitation frequency ν is shown in Fig. 6. Below 20 GHz no EPR signals have been observed which indicates the occurrence of the gap for resonance excitations $\Delta \approx 20$ GHz (0.7 cm^{-1}). It can be related to the magnetic anisotropy gap of the molecular complex which arises owing to the ZFS of the spin states of the molecular complex. Thus the gap Δ suggests a respective energy scale for magnetic anisotropy of the order of 1 cm^{-1} in agreement with the estimate of the ZFS parameter D from the static magnetic measurements.

An EPR spectrum comprising the main absorption peak and a weak satellite has been detected at 23.6 GHz (inset of Fig. 6) [30]. The intensity of the main peak strongly increases with increasing frequency whereas the satellite peak rapidly vanishes. The latter peak can be presumably attributed to a forbidden $\Delta S^z = \pm 2$ resonance transition between the spin states of the molecular complex which probably strongly decreases with increasing the magnetic field strength. The resonance field H_{res} of the strong absorption line defined as the field of the absorption maximum scales linearly with ν (Fig. 8). From the slope of the ν *versus* H_{res} dependence one obtains a g-factor value of 2.00 which is in conform with that expected for both Cr^{III} and high-spin Mn^{II}.

For excitation frequencies exceeding 170 GHz the EPR signal splits into two separate lines on the top of the broad dome-shaped background (Figs. 6 and 7). The signal can be well fitted as a sum of three Lorentzian lines. An example spectrum at $\nu = 350$ GHz and the corresponding fit are shown as an example in Fig. 7 where two sharp peaks are well reproduced by two narrow Lorentzian profiles whereas a third much broader Lorentzian line is required to model a broad background. From the fit one obtains the resonance fields of the two sharp lines which are plotted *versus* the excitation frequency in Fig. 8. The data points are located symmetrically with respect to the anticipated position of the low frequency single peak indicated by the dashed line in this figure. It is tempting to assign these two absorption lines to the individual resonances of Cr^{III} and Mn^{II} which may become resolved owing to the increase of the spectroscopic resolution with increasing magnetic field. The analysis of the static magnetic data yields a very weak exchange coupling between the paramagnetic ions, the strongest one being $|0.4|$ cm^{-1}. This result is consistent with the EPR observations because in this case one may expect that in magnetic fields of the order of a few Tesla the spins of Cr and Mn will process independently. If the respective g-factors are slightly different, the Cr and Mn EPR signals will split apart with increasing magnetic field. From the slope of the ν *versus* H_{res} dependences of the two lines one obtains the g-factors of 1.90 and 2.05 (Fig. 8).

One should note that owing to the ZFS both Cr^{III} and Mn^{II} may exhibit EPR spectra with the fine structures lines that, except for the nearly isotropic central line corresponding to the transition $|+1/2\rangle \leftrightarrow |-1/2\rangle$, depend on the direction of the magnetic field with respect to the principal axes of the metal ion—ligand cluster [31]. As a consequence, one would expect for the EPR spectrum of a polycrystalline sample comprising randomly oriented individual microcrystallites the angular averaging of the fine structure satellite peaks that would yield a broad background absorption topped with the sharp lines $|+1/2\rangle \leftrightarrow |-1/2\rangle$ of the respective species unaffected by powder averaging.

From the EPR data alone it is difficult at present to unambiguously conclude which of the two sharp resonances, nicely resolved in the EPR spectrum in strong magnetic fields, belong to Cr^{III} and Mn^{II}, respectively. The analysis of the susceptibility yields $g_{Mn} > g_{Cr}$ thus permitting to assign the left and the right peaks in Fig. 7 to the resonance of the decoupled Cr^{III} and Mn^{II} ions, respectively.

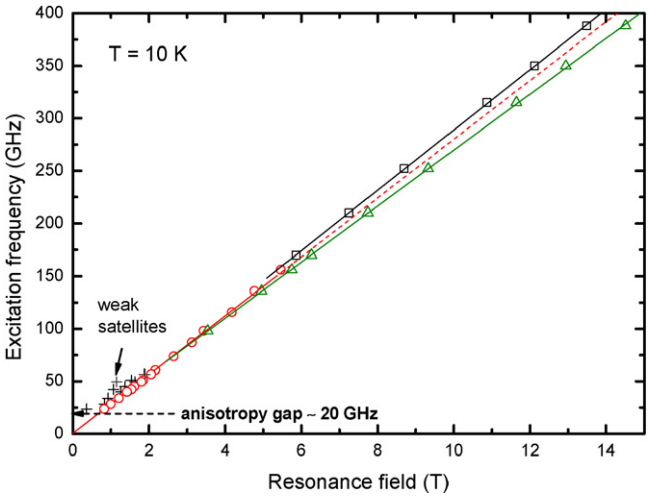

Fig. 8. ν *versus* H_{res} diagram: Circles and crosses correspond to the main peak and a weak satellite observed in the frequency domain $\nu < 170$ GHz. Squares and triangles correspond to the two sharp lines emerging in the spectrum at $\nu > 170$ GHz. Solid and dashed straight lines are fits to the data. A gap for resonance excitations is indicated by the dashed arrow. (for details see the text). Reproduced by permission of The Royal Society of Chemistry [29a].

Summarily, HF-EPR measurements are in accord with the weak antiferromagnetic coupling evaluated from the susceptibility measurements and indicate a value of $D \approx 1\,cm^{-1}$.

2.3. Concluding remarks and outlook

Although at the very outset it is clear that linear tetranuclear complexes of the type $M_AM_BM_BM_A$ are not good candidates for generating molecules with high-spins, they, because of their isostructural nature, are unique and ideally suited for the systematic study of intramolecular exchange interactions between four paramagnetic transition metal ions as a function of their respective d^n-electron configurations and the bridging groups.

That terminal Mn(IV)-ions in comparison to Cr(III) ions reduce the overall antiferromagnetic exchange between the central dimanganese(II) core by increasing the ferromagnetic components to the overall exchange is a noteworthy result of this study.

Thus, such isostructural complexes can improve our understanding of fundamental factors governing the magnetic properties of transition metal compounds. We emphasize in this respect that investigations of a series of isostructural polynuclear complexes with varying d^n-electron configurations are more informative in comparison to those comprising singly isolated exchange-coupled clusters only.

Our earlier observations of ferromagnetic interactions in an oximato-bridged $Cr^{III}Mn^{II}$ complex [32] led us to synthesize a star-shaped molecule with a small central spin and high peripheral spins; the central spin is expected to polarize the outer spins, thus resulting in a "high-spin" ground state. Unfortunately, this is not the case with $Cr^{III}Mn^{II}{}_3$, **6**, although with the targeted molecular spin topology. Thus, complex **6** is an example where the target molecule is synthesized but not with the desired magnetic properties, due to the atom-connections between the frustrated Mn(II) spins. In spite of a comparatively long Mn···Mn distance of 5.5 Å, an exchange-coupling path is prevailing between them irrespective of its weakness. This very weak coupling ($J_2 = -0.10\,cm^{-1}$) prevents the molecule to exhibit a "high-spin" ground state. In this particular case "spin frustration", contrary to our accepted notion, is not helpful for achieving high-spin molecules, thus suggesting a future direction of generating "high-spin" molecules.

3. Tetranuclear complexes based on polydentate amine-thiophenolate ligands

In an alternative approach, coordinatively unsaturated amine-thiophenolate complexes have been employed as elementary units for the preparation of polynuclear transition metal complexes with high-spin ground states. This part of the review will highlight the most important results originating from this work.

3.1. Synthetic approaches

3.1.1. Ligand design and synthesis

For the preparation of our binuclear building blocks we have employed a series of polydentate amine-thiophenolate ligands. The ligands HL^1 [33,34], H_2L^2 [35], H_2L^3 [36], H_3L^4 [37] and H_2L^5 [38] represent typical examples (Scheme 4). This section will focus specifically on the synthesis and coordination chemistry of the open chain ligands H_2L^1–H_2L^4. The work incorporating the chemistry of the hexaamine-dithiophenolate ligand H_2L^5 and related Schiff-base macrocycles can be found in recent reviews by Brooker [39], Schröder [40], Tamburini [41], and Kersting [42] and will therefore not be discussed further here.

The ligand HL^1 was prepared in three steps starting from the dialdehyde **7** as shown in Scheme 5. The procedure starts from the dialdehyde **7** [43] which reacts readily with potassium benzylthiolate in DMF to afford the thioether **8** in nearly quantitative yield. The thioether was subsequently converted to the corresponding dioxime **9** by reaction with hydroxylamine. The reduction and the deprotection of **9** in the final step could be accomplished with

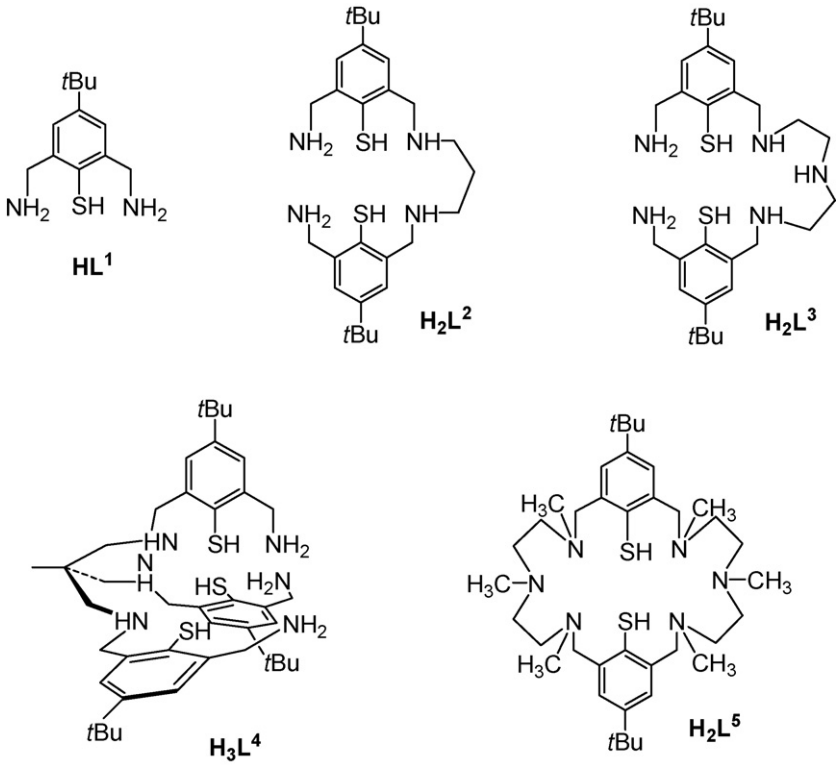

Scheme 4. Structure of the ligands H_2L^1–H_2L^5.

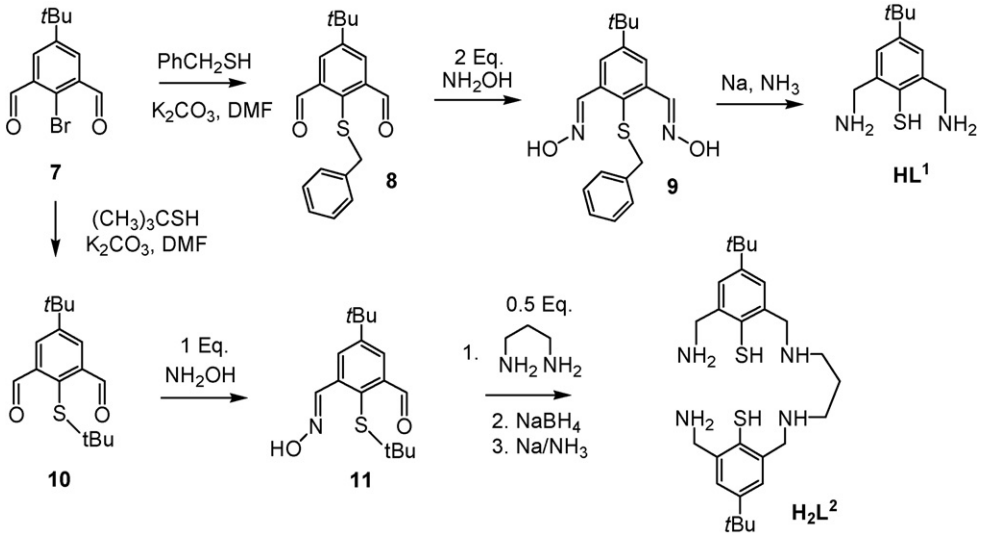

Scheme 5. Synthesis of HL^1 [33] and H_2L^2 [35].

sodium in liquid ammonia to provide the tridentate ligand HL^1 in 55% overall yield. A similar reaction sequence was employed to prepare the selenium derivative of HL^1 [44] and some of its alkylated variants [45].

The preparation of the hexadentate N_4S_2 ligand H_2L^2 was very similar to that of HL^1 (Scheme 5) [35]. Key step of this reaction sequence is the reaction of dialdehyde **10** with hydroxylamine in a 1:1 molar ratio, which affords the monoaldehyde **11** in good yields. Reaction of **11** with 1,3-diaminopropane in a 2:1 molar ratio followed by subsequent reductions with $NaBH_4$ and Na/NH_3 then provided H_2L^2 in good yields. The other polyamine-dithiophenolate ligands H_2L^3 and H_3L^4 were also prepared by this route and underline the broad scope of this reaction sequence [35,37,46]. When stored as their hydrochloride salts both HL^1 and H_2L^2 are air-stable and could be directly used for metal complex synthesis.

3.1.2. Coordination chemistry of amine-thiophenolates HL^1–H_2L^4

A large number of dinuclear metal complexes of the ligands HL^1–H_2L^4 have been synthesized and characterized within the past few years. Selected examples will now be presented and discussed.

The ligands HL^1 and H_3L^4 were found to support homo- (**12** [47], **13** [34], **14** [37], **15** [48]) as well as heterodinuclear complexes (**16** [49], **17**, **18** [37]) with a range of di- and trivalent metal ions (M = Cr, Fe, Co, and Ni). All complexes **12**–**18** have a face-sharing bioctahedral $N_3M(\mu\text{-}S)_3MN_3$ core structure as illustrated in Scheme 6 and were found to undergo two reversible one-electron transfer reactions. The potential ranges are neither exceptionally highly oxidizing nor reducing. This rendered possible the isolation of the corresponding $M^{II}M^{II}$, $M^{II}M^{III}$ and $M^{III}M^{III}$ forms and their structural and spectroscopic characterization (see next section).

The hexadentate ligand H_2L^2 also supports face-sharing bioctahedral complexes, but one bridging position and one terminal coordination site at each metal ion remains available for exogeneous ligand binding (Scheme 7). So far two coordination modes A and B of H_2L^2 have been observed. In the former coordination mode $(L^2)^{2-}$ wraps around the two metal ions in such a fashion that the coligands are *cis* to each other, whereas in the latter, a conformation is adopted in which the coligands are mutually *trans* [50].

The bridging and terminal coordination positions in the $[M_2(L^2)(\mu\text{-}L')(L')_2]^{n+}$ can be occupied by the same or by different coligands as illustrated by the series of dinuclear Cr^{III} complexes **19**–**22** (Scheme 8). Thus, reaction of $Cr^{II}Cl_2$ with H_2L^2 in methanol in the presence of base followed by air-oxidation afforded a 70:30 mixture of the chloro/hydroxo species *cis*,*cis*-$[Cr^{III}_2(L^2)(\mu\text{-}OH)(Cl)_2]^+$ (**19**) and *trans*,*trans*-$[Cr^{III}_2(L^2)(\mu\text{-}OH)(Cl)_2]^+$ (**20**) [50]. In each case the Cr^{III} ions are in a distorted octahedral environment, being coordinated by two bridging S and two N atoms from $(L^2)^{2-}$ and one terminal Cl^- and one bridging OH^- ion (Fig. 9). The Cr·Cr distance is 2.905(1) Å in **19** and 2.913(2) Å in **20**. Reaction of the hydroxo-bridged complexes with HCl yielded the chloro-bridged cations *cis*,*cis*-$[Cr^{III}_2(L^2)(\mu\text{-}Cl)(Cl)_2]^+$ (**21**) and *trans*,*trans*-$[Cr^{III}_2(L^2)(\mu\text{-}Cl)(Cl)_2]^+$ (**22**), respectively. The bridge substitution reactions proceed in each case with retention of the structures of the parent complexes.

Several nickel(II) complexes have also been obtained by employing the N_4S_2 ligand H_2L^2 [35,51]. Thus, while treatment of the coordinatively unsaturated complex **23** with pyridazine (*pydz*) followed by addition of two equivalents of NH_4SCN affords a dinuclear μ-pyridazine complex $[Ni^{II}_2(L^2)(\mu\text{-}pydz)(NCS)_2]$ (**24**), the reaction of **23** with pyridazine/NaN_3 gave a tetranuclear nickel(II) complex $[\{Ni^{II}_2(L^2)(\mu\text{-}pydz)(N_3)\}_2][BPh_4]_2$ (**25**) (Scheme 9). In complex **24** two *fac*-$(SCN)N_2Ni^{II}$ units are bridged by two S and a $\mu_{1,2}$-*pydz* unit at a Ni···Ni distance of 3.340(1) Å. Complex **25**, on the other hand, is composed of two binuclear $[Ni_2(L^2)(\mu\text{-}pydz)]^{2+}$ subunits which are linked by two azide ions to give a rectangular array of four six-coordinate Ni^{II} ions. These results have thus established the ability of the binuclear complexes to function as building blocks for higher nuclearity species.

The coordination chemistry of the septadentate H_2L^4 has also been investigated. The complexes $[Ni_2(L^4)Cl]Cl$ (**26**) and $[Ni_2(L^4)(NCS)](OH{\cdot}OH_2)$ (**27**) differ from the above complexes in that they have central $N_2Ni(\mu\text{-}S)_2NiN_3L'$ (L′ = Cl, NCS) core structures with dithiolate-bridged NiN_2S_2 and six-coordinate NiN_3S_2L' units as illustrated in Scheme 10.

3.2. Structural and spectroscopic characterization

Most of the complexes described in Section 3.1.2 have been characterized by X-ray-crystallography and to get further insight into their electronic structures also by spectroscopic methods (UV/Vis, EPR, Mößbauer spectroscopy) and temperature-dependent magnetic susceptibility measurements. In the following selected examples will be discussed.

EPR spectroscopic studies and temperature dependent magnetic-susceptibility measurements unambiguously reveal that intramolecular magnetic exchange interactions exist between

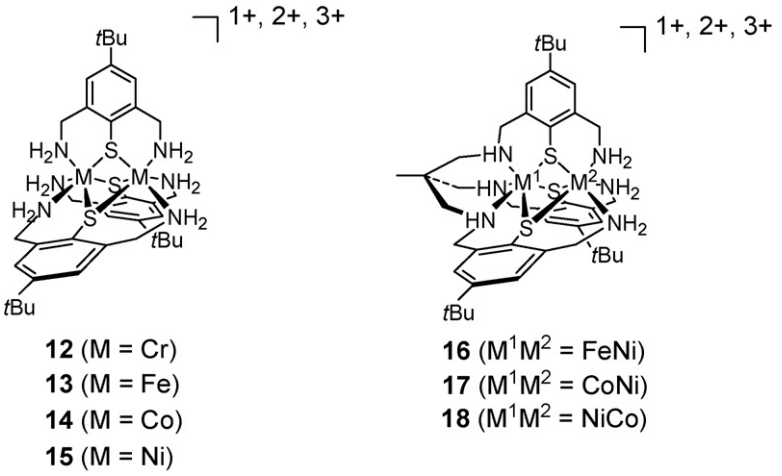

Scheme 6. Structure of the complexes **12**–**18**.

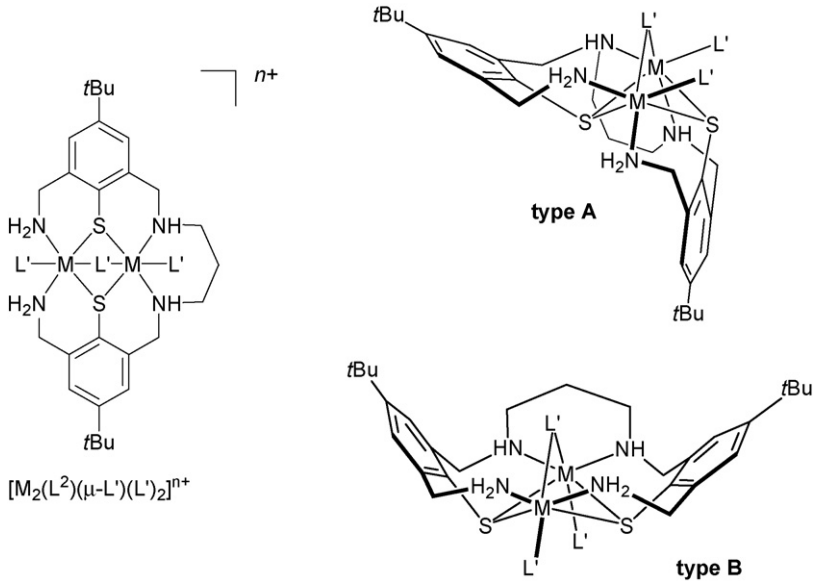

Scheme 7. Schematic representation of the two binding modes of the N_4S_2 ligand $(L^2)^{2-}$ in bioctahedral $[M_2(L^2)(\mu\text{-}L')(L')_2]^+$ complexes (L′ = bridging or terminal coligand).

the paramagnetic metal ions in **12**–**18**. The exchange interactions can be antiferromagnetic or ferromagnetic in nature. The $Cr^{III}Cr^{III}$-Komplex $\mathbf{12}^{3+}$ with a d^3d^3-electronic configuration, for example, exhibits a $S = 0$-ground state ($J = -39\,cm^{-1}$, $\mathbf{H} = -2JS_1S_2$) [47]. The mixed-valent $Ni^{II}Ni^{III}$ complex $\mathbf{15}[BPh_4]_2$, on the other hand, exhibits an $S = 3/2$ ground state that is attained by a strong intramolecular ferromagnetic exchange interaction between a low-spin Ni^{III} ($S = 1/2$) and a Ni^{II} ($S = 1$) ion (Fig. 10a and b) [52]. J was found to be equal to $86\,cm^{-1}$ in this case ($\mathbf{H} = -2JS_1S_2$). The heterodinuclear $Ni^{II}Fe^{III}$ complex $\mathbf{16}^{2+}$ was investigated by X-ray crystallography, ^{57}Fe-Mößbauer and EPR spectroscopy [49]. The short average Fe–N (2.047(4) Å) and Fe–S (2.291(1) Å) distances and the single quadrupole doublet with $\delta = 0.26\,mm\,s^{-1}$ are indicative of the presence of a low-spin Fe^{III} ion, a fact that corroborates nicely with results reported by Wieghardt and coworkers for a set of related Fe^{III} complexes with N_3S_3 coordination [53,54]. The 77 K

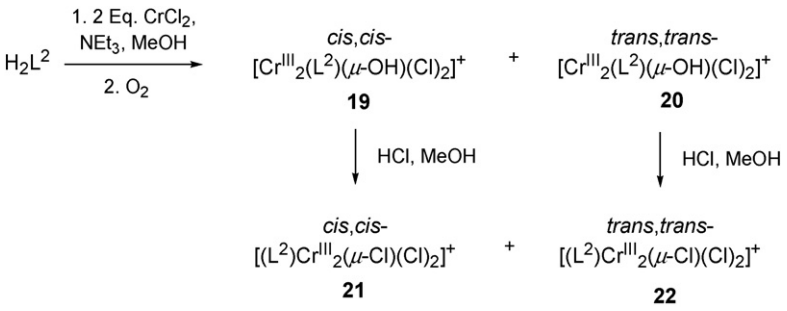

Scheme 8. Synthesis of **19**–**22** [50].

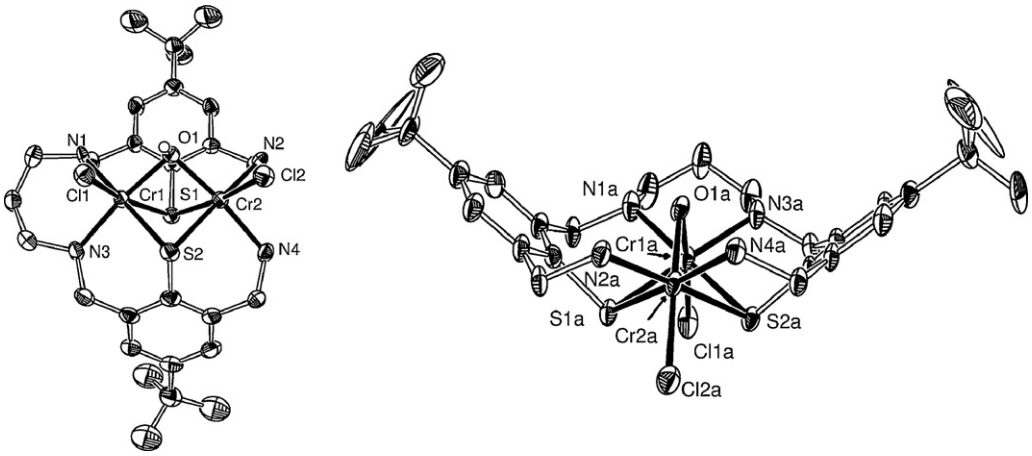

Fig. 9. Molecular structures of **19** (left) and **20** (right) in the crystal. This figure was generated using data downloaded from The Cambridge Crystallographic Data Centre (CCDC) and corresponds to the structures originally reported in Ref. [50].

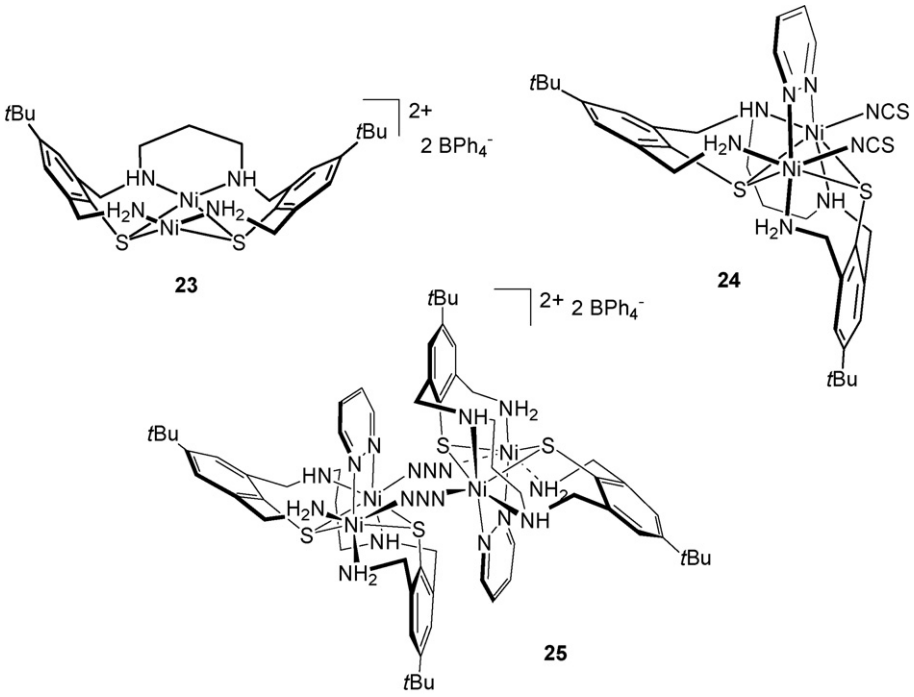

Scheme 9. Schematic representation of the structures of the nickel(II) complexes **23**–**25** [51].

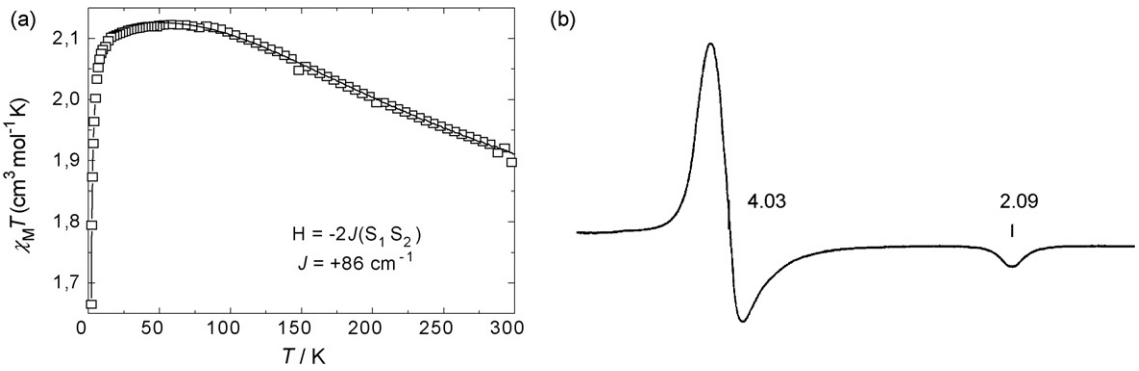

Fig. 10. (a) Plot of $\chi_M T$ against T for **15**·2BPh$_4$. The full line represents the best theoretical fit [52]. (b) EPR powder spectrum of **15**·2BPh$_4$ at 77 K, apparent g values are indicated [48].

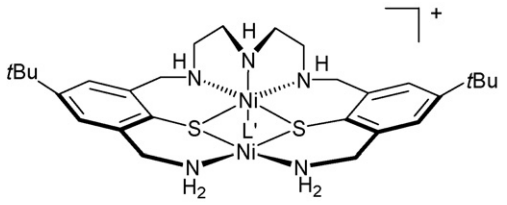

$[Ni_2(L^4)(Cl)][Cl]$ (**26**, L' = Cl)
$[Ni_2(L^4)(NCS)][H_2O{\cdot}OH]$ (**27**, L' = NCS)

Scheme 10. The structures of the dinickel(II) complexes **26** and **27** [36].

EPR powder spectrum of $\mathbf{16}^{2+}$ and the room temperature magnetic moment of 2.3 μ_B are indicative of an $S = 1/2$ spin ground state which is most likely attained by an intramolecular antiferromagnetic exchange interaction between the Ni^{II} ($S_1 = 1$) and a low-spin Fe^{III} ($S = 1/2$) ion. Further such studies are still required to study the metal–metal interactions as a function of the metal oxidation state and to set up magneto structural correlations for these interesting class of complexes.

As mentioned in Section 3.1.2, it has been possible to use the binuclear complexes as building blocks for polynuclear complexes. Moreover, this approach allows for the construction of polynuclear complexes with high-spin ground states. The two complexes **24** and **25** provide representative examples. The temperature-dependence of the molar magnetic susceptibility of both complexes have been examined between 2 and 300 K by using a SQUID magnetometer. Fig. 11 shows the results in the form of $\chi_m T$ *versus* T plots. Least-squares fits of the magnetic susceptibility data by full-matrix diagonalization of the appropriate spin Hamiltonians below provided the J and g values for each compound [51].

$$\hat{H} = -2J\hat{S}_1\hat{S}_2 + \sum_{i=1}^{2}(D\hat{S}_{iz}^2 + g_i\mu_B B\hat{S}_{iz}) \quad (\text{for } \mathbf{24})$$

$$\hat{H} = -2J_1(\hat{S}_1 \cdot \hat{S}_2 + \hat{S}_3 \cdot \hat{S}_4) - 2J_2(\hat{S}_2 \cdot \hat{S}_3 + \hat{S}_1 \cdot \hat{S}_4) + \sum_{i=1}^{4}(D\hat{S}_{iz}^2 + g_i\mu_B B\hat{S}_{iz}) \quad (\text{for } \mathbf{25})$$

For the dinuclear building block **24** the parameters $J = 11.5\ cm^{-1}$ and $g = 2.15$ were obtained. For the centrosymmetrical complex **25**, the best fit to the data yielded two ferromagnetic coupling constants $J_1 = 6.47\ cm^{-1}$ (intradimer coupling constant) and $J_2 = +3.59\ cm^{-1}$ (interdimer coupling constant via the azide bridges), a g value of 2.11 and a zero-field splitting parameter $D = -0.068\ cm^{-1}$ [55]. The ferromagnetic coupling between the nickel ions in the Ni^{II}–($\mu_{1,3}$-N_3)–Ni^{II} fragment in **25** is rather atypical. In general, all binuclear Ni compounds with this motif are known to exhibit antiferromagnetic interactions. Escuer et al. have shown that the magnitude of the antiferromagnetic exchange coupling constant depends on the Ni–N–N bond angle as well as on the Ni–N–N–N–Ni torsional angle. If the former angle exceeds 155° and (or) the latter 55° the exchange interactions become ferromagnetic [56]. Our observation of a weak ferromagnetic coupling in **25** showing a large Ni–N–N–N–Ni torsional angle of 76.4° is in good agreement with this trend (for the drastic influence of Ni–N–N–N–Ni torsion on the type and magnitude of magnetic coupling see also Section 4 of this review). Thus, the building block **24** exhibits an $S = 2$ ground state, while the tetranuclear complex **25** is characterized by an $S_T = 4$ spin ground state. From a formal point of view, the $S_T = 4$ ground state of **25** results from an addition (not subtraction) of the pair states of the two constituent subunits **24**. HF EPR spectroscopic measurements further reveal that **25** has an appreciable magnetic anisotropy of $S_{tot}^2\left|D\right| \sim 3.5\ cm^{-1}$ ($S_{tot} = 4$, $D = -0.21\ cm^{-1}$) [55], i.e. a magnetically bistable ground state has been realized (see Section 3.3). Thus, a novel approach to polynuclear complexes with high-spin ground states has been developed.

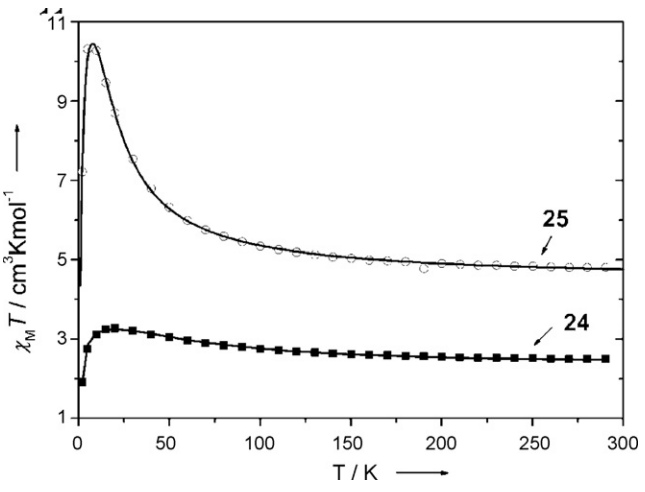

Fig. 11. Plots of $\chi_M T$ against T for **24** and **25**. The full line represents the best theoretical fit [51].

3.3. High-frequency high-field EPR and pulsed-field magnetization

Magnetic properties of compound **25** which contains in the molecular core four Ni(II) ions each possessing a spin $S_{Ni} = 1$ coupled magnetically into a four-spin cluster have been studied in more detail by means of high-field static magnetization measurements and high-frequency high-magnetic field electron spin resonance (HF-EPR). The static magnetization has been measured with a SQUID magnetometer from Quantum Design in fields up to 5 T and with a pulsed-field magnetometer operating up to 55 T in the National pulsed magnetic field laboratory in Toulouse [57]. For technical details of the HF-EPR setup enabling EPR measurements at frequencies ν from 20 GHz up to 800 GHz in magnetic fields up to 17 T see Ref. [30].

3.3.1. Static magnetization measurements

In Fig. 12 the temperature dependent part of the inverse susceptibility $1/\chi$ is plotted *versus* temperature. The inset shows a perfectly linear behavior of the curve between 80 and 340 K. This high temperature domain has been fitted with a Curie–Weiss law $\chi = C/(T - \Theta_{Weiss})$. The fit yields a Curie–Weiss constant $C = 3.66$ emu/mol which gives an effective moment of 5.4 μ_B. Here μ_B is the Bohr magneton. This moment corresponds to an effective spin $S_{eff} = 2$, if a typical g-factor of 2.2 for nickel is assumed [58] (a precise determination of the g-factor from HF-EPR yields the value of 2.16, see below). The positive sign of the Weiss temperature $\Theta_{Weiss} \sim 17$ K indicates a ferromagnetic (FM) exchange in the spin cluster.

The main panel of Fig. 12 gives a more detailed view of the low temperature domain $T < 80$ K. Since the slope of the χ^{-1} curve is proportional to the inverse effective magnetic moment μ_{eff}^{-1} of the four-spin cluster, its deviation from the Curie–Weiss fit in this temperature region provides additional information about the evolution of the magnetic state of the cluster at low temperatures. In particular, a decrease of the slope of $\chi(T)^{-1}$ corresponds to an increase of μ_{eff}. Therefore one can conjecture that the total spin of

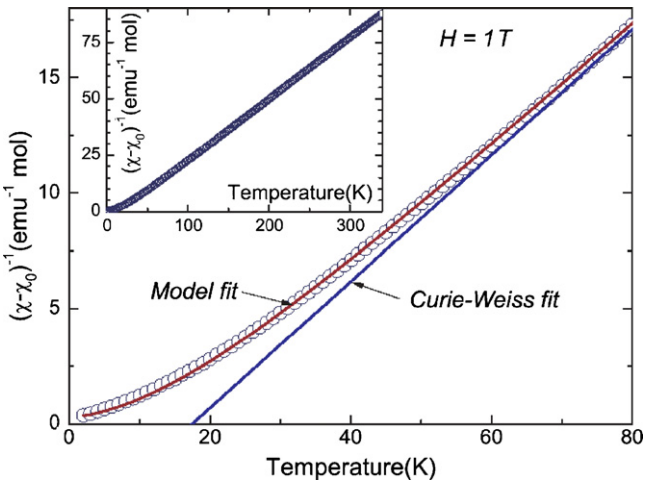

Fig. 12. Inverse static magnetic susceptibility, $(\chi(T)-\chi_0)^{-1}$, of compound **25**. χ_0 is the temperature independent part comprising diamagnetic and Van-Vleck contributions. *The inset* demonstrates the linear behavior of the inverse susceptibility in a wide temperature range which follows perfectly a Curie–Weiss law at $T > 80$ K. *Main panel*: Inverse susceptibility (circles), fit to a Curie–Weiss law (blue solid line), and the fit of a J_1J_2-model (red solid line) in the low temperature range (for details see the text).

the cluster in the ground state is larger than the high temperature estimate $S_{eff} = 2$.

The insight into the magnetism of the ground state can be obtained by measurements of the magnetization M as a function of magnetic field at low temperatures. However, it was not possible to achieve full saturation of the magnetization M_{sat} of compound **25** with the SQUID magnetometer operating in fields up to 5 T. As is evident from inset of Fig. 13 M still continues to increase by approaching a maximum field of 5 T. To address directly this question measurements of M_{sat} have been performed in pulsed fields up to 50 T [57]. The main result is shown in Fig. 13. A plateau of M at the level of 8.8 μ_B is achieved in fields larger than ~10 T. Taking the g-factor value $g = 2.16$ from the HF-EPR measurements (see below) and recalling that M_{sat} is given by a product of g and the spin S as $M_{sat} = gS$ one obtains the total spin of the four-spin cluster $S_{tot} = 4$. Therefore one can conclude that in compound **25** all four Ni(II) spins are coupled FM which yields at low temperatures a highly magnetic ground state with a highest possible spin value of 4.

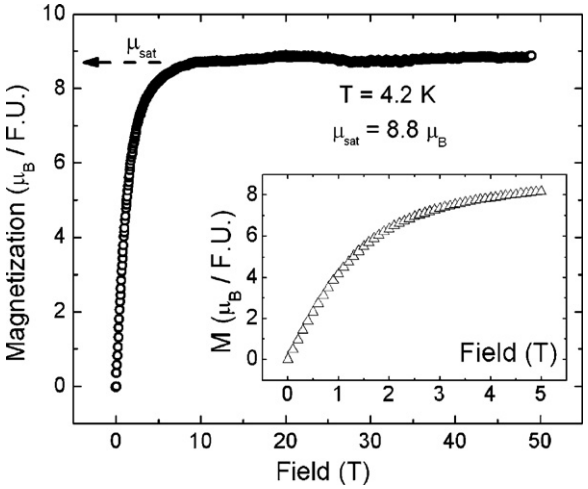

Fig. 13. Field dependence of the magnetization M of compound **25** at a low temperature of 4.2 K. Inset: Low field data obtained with the SQUID magnetometer. M does not saturate at the highest achievable field of 5 T. *Main panel*: Measurement in pulsed fields up to 50 T. The saturation value $M_{sat} = 8.8\ \mu_B$ is achieved above ~10 T.

3.3.2. High-frequency high magnetic field EPR spectroscopy

Valuable information about the properties of the ground state of compound **25** has been obtained from measurements of HF-EPR in a broad range of temperatures, magnetic fields and excitation frequencies ν. Owing to a large number of spin levels $|S^z\rangle$ in the ground state, $S^z = -4 \cdots 4$, whose degeneracy can be partially lifted even in the absence of the external magnetic field due to a combined action of the ligands' crystal field and the spin–orbit coupling (so-called zero field splitting, ZFS, see Ref. [57]) one would expect an EPR spectrum comprising multiple resonance lines. Indeed measurements of a powder sample of **25** pressurized in a pellet reveal a fine structure of the spectrum which can be assigned to resonance transitions between different spin levels within the ground state $S_{tot} = 4$ multiplet. An example spectrum at $\nu = 76$ GHz and $T = 3$ K is shown in Fig. 14. The fine structure of the spectrum comprising up to 8 features labeled from a to h (see arrows and associated labels in Fig. 14) can be clearly identified. As can be seen in Fig. 14 the position in field H^i_{res} of resonances $i = a..h$ depends on the excitation frequency ν. The relation between H^i_{res} and ν (so-called resonance branch) is linear for all resonance peaks. The g-factor in the ground state can be determined from the slope of the branches $g = (h/\mu_B)\partial\nu/\partial H^i_{res} = 2.17$. Here h is the Planck constant. The branch a intersects the frequency axis at ~40 GHz (1.33 cm^{-1}). It identifies the maximum microwave energy compared to the intersections of other branches b–h and, therefore, gives a first estimate of the magnitude of the ZFS of the spin levels $\Delta \sim 1.33\ cm^{-1}$. As will be discussed below, the associated resonance a belongs to the lowest transition in the $S_{tot} = 4$ multiplet which can be referred to as $|-4\rangle \leftrightarrow |-3\rangle$.

Further insights into the structure of the ground state spin levels $|S^z\rangle$ have been obtained from HF-EPR measurements of an oriented sample of compound **25** whose powder particles (individual crystallites) were aligned in the magnetic field along their magnetic anisotropy axis ("easy axis"). Experiments have been carried out at a constant frequency $\nu = 360$ GHz in a temperature range 5–130 K.

In contrast to the powder spectra (Fig. 14), the spectra of the oriented sample, shown in Fig. 15a, reveal up to six well resolved resonance signals. The peaks, numbered 1–6 in the figure, are almost equally spaced by $\delta H_{res} \sim 0.43$ T and can be associated with dedicated spin transitions $|S^z\rangle \leftrightarrow |S^z \pm 1\rangle$. One can notice a

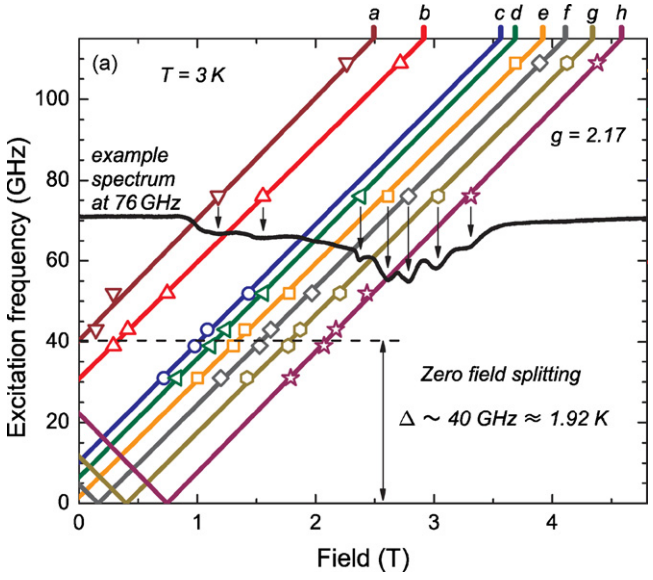

Fig. 14. The frequency dependence of EPR fine structure peaks a–h from powder spectra at 3 K. The peaks are marked by arrows in a representative HF-EPR spectrum at 76 GHz. The slope of the branches ν *versus* H^i_{res}, $i = a..h$, yields the g-factor $g = 2.17$. The intercept of branch a with the frequency axis gives an estimate of the ZFS gap $\Delta \sim 1.92$ K (or 1.33 cm^{-1}) (see the text for details).

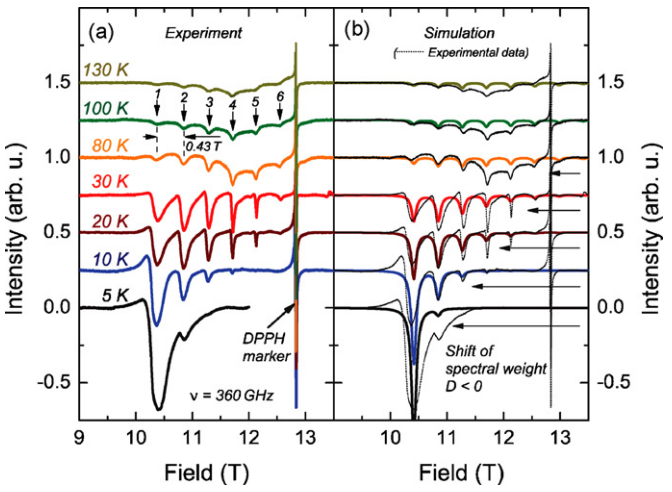

Fig. 15. (a) Temperature dependence of experimental HF-EPR spectra of the oriented powder sample at $\nu = 360$ GHz. Depending on temperature up to 6 equally spaced resonance peaks with spacings $\delta H_{res} \sim 0.43$ T are observed. Sharp peak at 12.9 T is due to the DPPH field marker. (b) Simulated spectra (thick colored lines) in comparison with the experimental results (thin dotted lines). Note a significant redistribution of the spectral weight with temperature which is very well reproduced in the model spectra assuming a negative sign of the magnetic anisotropy.

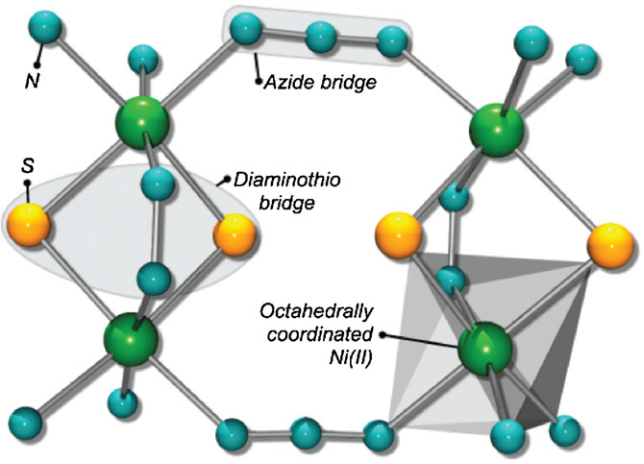

Fig. 16. Structure of the magnetic core of compound **25**. The vertical diaminothio-bridged binuclear building blocks are horizontally linked by μ-azide ligands. Each Ni(II) ion, $S_{Ni} = 1$, is surrounded by ligands in a pseudo octahedral coordination.

remarkable redistribution of the spectral weight upon changing the temperature. While resonance 1 is observed even at 5 K, the resonances 2–6 are successively activated with raising temperature. Thus resonance 1 is due to the resonance excitation from the $|S^z\rangle$ state lowest in energy, whereas resonances 2, 3 etc. correspond to the resonance transitions from higher energy states within the $S_{tot} = 4$ multiplet. As will be discussed in the next section resonance 1 is due to the ground state excitation $|-4\rangle \leftrightarrow |-3\rangle$, resonance 2 arises from the first excited state $|-3\rangle \leftrightarrow |-2\rangle$ etc.

3.3.3. Discussion of the magnetic data

The static magnetic and HF-EPR data can be successfully interpreted in the framework of the relevant spin Hamiltonian H_{spin} which comprises several contributions:

$$H_{spin} = J_1(\mathbf{S}_1\mathbf{S}_3 + \mathbf{S}_2\mathbf{S}_4) + J_2(\mathbf{S}_1\mathbf{S}_2 + \mathbf{S}_3\mathbf{S}_4) + D_{sia}\sum_{i=1..4}[S_{iz}^2 - 1/3S_{Ni}(S_{Ni}+1)] + g\mu_B\mathbf{H}\sum_{i=1..4}\mathbf{S}_i.$$

Considering the topology of the magnetic core of compound **25**, shown in Fig. 16, the four Ni spins $S_{Ni} = 1$ are assumed to be coupled as sketched in Fig. 17. The coupling between the Ni centers of the dinuclear building blocks is described by the isotropic coupling parameter J_1 and the coupling mediated by the azide bridge is denoted as J_2. In addition to this isotropic Heisenberg exchange (first two terms of H_{spin}), the spin Hamiltonian comprises further terms for the energy of the magnetic (single ion) anisotropy (third term of H_{spin}) and the Zeeman energy of interaction of spins $\mathbf{S}_i$ ($i = 1..4$) with an external magnetic field $\mathbf{H}$ (forth term of H_{spin}). The single ion anisotropy (SIA) arising due to the crystal field effect is quantified by a parameter D_{sia} which is usually the dominant lowest order term for a tetragonally distorted pseudo-octahedral metal center environment.

The static magnetic susceptibility $\chi(T)$ can be modeled by taking the second field derivative of the Hamilton operator H_{spin}:

$$\chi(T) = \partial^2[H_{spin}(H, J_1, J_2, g, D_{sia})]/\partial H^2 + C_{imp}/T + \chi_0.$$

Here C_{imp}/T is a small paramagnetic impurity term and χ_0 accounts for temperature independent diamagnetic and Van-Vleck contributions. Both the g-factor value and D_{sia} can be taken from HF-EPR measurements. From the frequency dependence of the HF-EPR fine structure (Fig. 14) the g-value amounts to 2.17 and D_{sia} is, in fact, given by the ZFS gap $\Delta = D_{sia} = 1.33\ cm^{-1}$ (the refined values amount to $g = 2.16$ and $D_{sia} = 1.51\ cm^{-1}$, see below). By tuning the exchange parameters J_1 and J_2 one can obtain a good agreement with experimental susceptibility data taking $J_1 \sim -11\ cm^{-1}$ and $J_2 \sim -5.6\ cm^{-1}$ (solid red line in Fig. 12). The negative, i.e. FM, sign of both coupling constants nicely confirms the experimental observation that at low temperatures all four Ni spins form a total $S_{tot} = 4$ ground state.

The analysis of the EPR excitations in the ground state $S_{tot} = 4$ multiplet of compound **25** can be performed with a reduced spin Hamiltonian H_{spin}^{red} which neglects the high energy spin multiplets $S_{tot} = 3$, 2, 1 and 0. It reads

$$H_{spin}^{red} = D_{mol}[S_{tot}^{z2} - (1/3)S_{tot}(S_{tot}+1)] + g\mu_B\mathbf{H}\mathbf{S}_{tot}.$$

Remarkably, such a reduction changes the scale of the parameter D, so that $D_{mol} \neq D_{sia}$. However, both parameters are related such that by setting $D_{mol} = D_{sia}/[S_{tot}^2 - S_{tot} - 1)^2]$ yields the correct value of the ZFS $\Delta = 7D_{mol}$ from the EPR experiment in this case (see Refs. [58,59]).

Fig. 18 shows an example of the resulting spin level scheme. The field dependence of the spin states $|S^z\rangle$ is obtained from the diagonalization of H_{spin}^{red}. The sign of the magnetic anisotropy D_{mol} has been chosen negative. The ZFS complies with the gap Δ between the spin doublet states $|\pm4\rangle$ and $|\pm3\rangle$. The figure shows also the simulation of an EPR spectrum for $\nu = 50$ GHz and $T = 8$ K. The spectrum

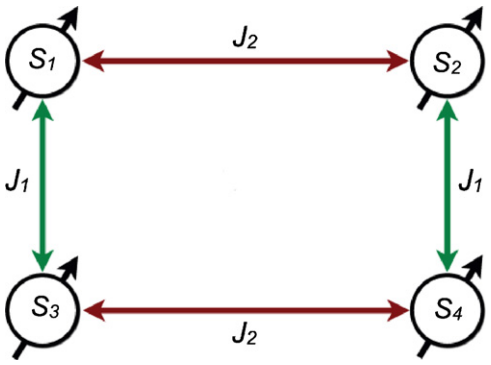

Fig. 17. FM coupling scheme of compound **25**. J_1 is the coupling of Ni spins in binuclear fragments S_1, S_3 and S_2, S_4. J_2 is the coupling between two FM dimers in the four-spin cluster.

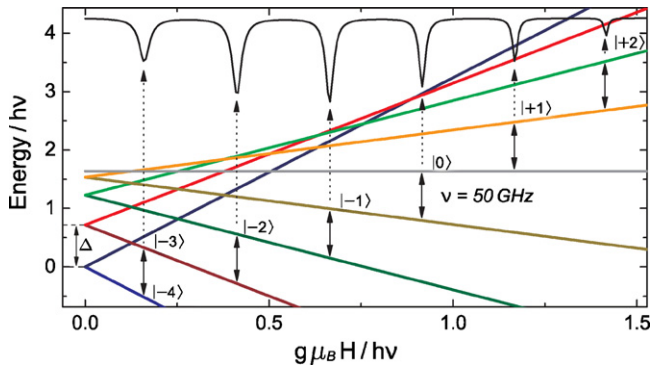

Fig. 18. Spin levels for $S_{tot} = 4$ with a negative uniaxial anisotropy parameter $D_{mol} = \Delta/7 = -0.21\ cm^{-1}$ and $g = 2.16$ in an external field H parallel to the magnetic anisotropy axis. A simulated EPR spectrum is plotted as an example for the excitation frequency $\nu = 50$ GHz. Note a bistable ground state $|\pm 4\rangle$ for H = 0.

is composed of Lorentzian line profiles. The line intensities were scaled according to the respective transition probabilities weighted by the thermal population of the spin states $|S^z\rangle$ within the ground state multiplet $S_{tot} = 4$.

The fact that in compound **25** a bistable magnetic ground state $|S^z = \pm 4\rangle$ is realized is nicely confirmed by the modeling of the temperature evolution of HF-EPR spectra (see Fig. 15b). At low temperatures predominantly the doublet $|\pm 4\rangle$ state is populated. Therefore only the low-field resonance line due to the transition $|-4\rangle \leftrightarrow |-3\rangle$ has an appreciable intensity. With increasing temperature the population of the state $|-3\rangle$ increases and therefore the next line associated with the transition $|-3\rangle \leftrightarrow |-2\rangle$ grows. This development continues until the population of all $|S^z\rangle$ states of the ground state $S_{tot} = 4$ multiplet nearly equalizes and the spectrum acquires a symmetric shape. A very good agreement of the model spectra with the experimental ones justifies the correctness of the chosen parameters [60]. In particular, the modeling enables to refine the magnitude of the g-factor and ZFS $\Delta = 7D_{mol}$, yielding the values $g = 2.16$ and $\Delta = 1.51\ cm^{-1}$. With these values one can calculate the spacing between the neighboring lines in the EPR spectrum $\delta H_{res} = 2|D_{mol} \times 20.8\ GHz\ K^{-1}|/14g = 0.426\ T$ which is in a very good agreement with the experimental spacing $\delta H_{res} = 0.43$ T (cf. Fig. 15a).

The magnetic anisotropy energy of the magnetic core of compound **25** i.e. a potential energy barrier which separates the degenerate states $|-4\rangle$ and $|+4\rangle$, is of the order $|D_{mol}|S^2_{tot} \sim 3.5\ cm^{-1}$. This sets a respective low temperature scale for realization of magnetic bistability as well as quantum tunneling and slow magnetic relaxation processes which are remarkable fingerprints of single molecular magnets. The quest of these phenomena in compound **25** which requires experiments at subKelvin temperatures is currently in progress.

3.4. Conclusion and perspectives

The above results clearly show that discrete binuclear complexes of binucleating polyaza-thiophenolate ligands can be used as building blocks for the construction of polynuclear complexes with high-spin ground states. The ground states of the binuclear subunits can be controlled by the choice of the metal (M^{n+}), the coligand (L'), and the metal oxidation state (n). The bridging ligands can mediate magnetic exchange interactions between the individual subunits, such that high-spin ground states can be attained. This is a new design principle for the construction of high-spin molecules. We think that further development of these prototypes can lead to new molecular-based magnetic materials and that we can contribute to

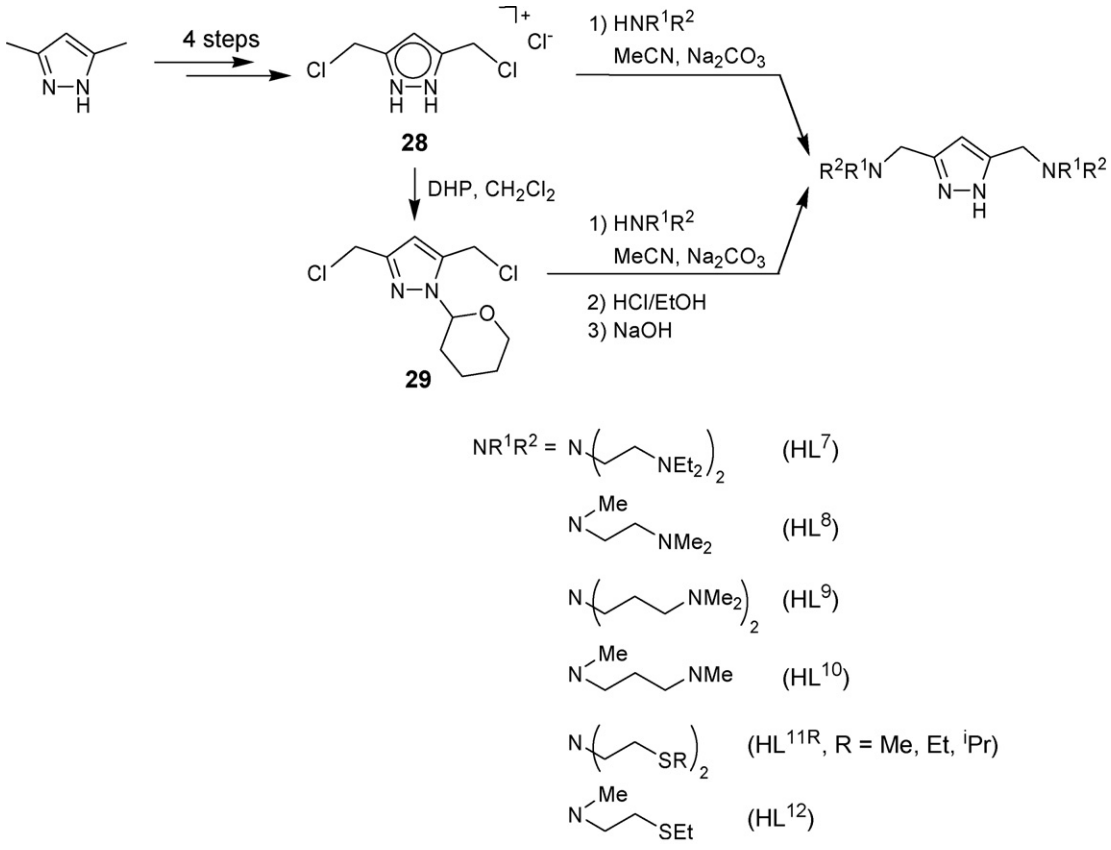

Scheme 11. Synthesis of ligands HL^7–HL^{12}.

an understanding of the factors that govern the molecular magnetic relaxation process.

4. Tetranuclear complexes from pyrazolate-based binucleating scaffolds

Successful strategies for obtaining (in a targeted manner) stable and well-defined bi- and multinuclear complexes generally rely on compartmental ligand scaffolds that provide distinct binding pockets for the metal ions. As shown in Section 3, this approach is becoming increasingly popular in the field of molecular magnetism, since the bi- and oligometallic complexes may serve as valuable building blocks for the controlled assembly of larger clusters and extended spin systems with particular spin topologies [61]. Pyrazolate-based binucleating ligands have proven very useful for nesting two metal ions [62]. The scope of modulating electronic and geometric characteristics of the bimetallic core by varying the ligand side arms attached to the 3- and 5-positions of the heterocycle is an attractive option for this class of ligands. Important variations comprise the type and number of side-arm donor atoms as well as the lengths of the chelate arms. While the former allows for the modification of the coordination numbers and electronic structures of the metal ions, the latter controls the properties of the bimetallic pocket, including the metal–metal distance [63]. This part of the review summarizes the results that have been obtained in nickel/azide chemistry using such pyrazolate ligands, with a focus on tetranuclear systems.

4.1. Synthetic approaches

A series of pyrazolate-based ligands HL^7–HL^{12} has been used in the present context (Scheme 11). These ligands contain either tertiary amine donors (HL^7–HL^{10}) or thioether donors (HL^{11}, HL^{12}) in the chelate arms, and they differ by the number of donor atoms (HL^7 *versus* HL^8, HL^9 *versus* HL^{10}, and HL^{11} *versus* HL^{12}) and by the length of the arms (HL^7 *versus* HL^9, HL^8 *versus* HL^{10}). All ligands are conveniently prepared from 3,5-bis(chloromethyl)pyrazole **28**, which can be synthesized in four steps from commercial 3,5-dimethylpyrazole [64], via nucleophilic substitution by the corresponding side arm amine under basic conditions [63]. Since the pyrazole-NH exhibits some competing nucleophilicity, however, the products prepared via this route often contain small amounts of unwanted oligomeric or polymeric side products, which are hard to separate. Products with higher purity can be obtained when the *N*-tetrahydropyranyl protected derivate **29** is employed as the key starting material [65].

The syntheses of dinickel(II) azido complexes of the various ligands are straightforward and usually do not require anaerobic conditions. In a typical procedure, the respective ligand precursor is treated with one equivalent of base (such as KO^tBu) in polar organic solvents (such as MeOH), and two equivalents of the nickel salt (such as $Ni(ClO_4)_2{\cdot}6H_2O$) are then added, followed by the appropriate equivalents of NaN_3. While complex formation is conveniently confirmed by mass spectrometry (showing the fragment $[LNi_2(N_3)_x]^+$) or by IR spectroscopy (with characteristic bands for the $\nu(N_3)$ stretches around 2100 cm^{-1}), crystallization and X-ray crystallographic characterization of the resulting complexes is crucial for understanding their magnetic properties. Single crystals can usually be obtained by slow diffusion of diethyl ether or light petroleum into solutions of the complexes in polar organic solvents such as MeOH, acetone, DMSO, or MeCN. If appropriate, additional coligands (such as acetate) can be added at any point of the synthetic sequence.

4.2. Structural and spectroscopic characterizations

4.2.1. The dinickel(II) building blocks

Representative examples of dinickel(II) complexes of the various pyrazolate ligands are collected in Scheme 12. In all cases the two metal ions are hosted within the adjacent binding pockets of the ligand scaffold, and an azide ion is found within the resulting bimetallic pocket [66]. As shown previously for ligands containing a central pyrazolate unit [63,67], the lengths of the chelate arms in the 3- and 5-positions of the heterocycle determines the preferred range of metal–metal separations that is supported by the binucleating scaffold: longer N-donor arms that give six-membered chelate rings allow the two metal ions to approach rather closely at ~3.5 Å. This is most suitable for the azide to adopt the μ-1,1 (*end-on*) bridging mode in, e.g., **30**. Shorter N-donor chelate arms pull the two metal ions back and apart to enforce larger metal–metal distances, usually above 4 Å. This distance necessarily leads to the μ-1,3 (*end-to-end*) bridging of the azide in, e.g., **31** [66]. Because of the longer Ni–S bond lengths, thioether donors in the ligand side arms lead to a borderline situation that enables both different azide binding

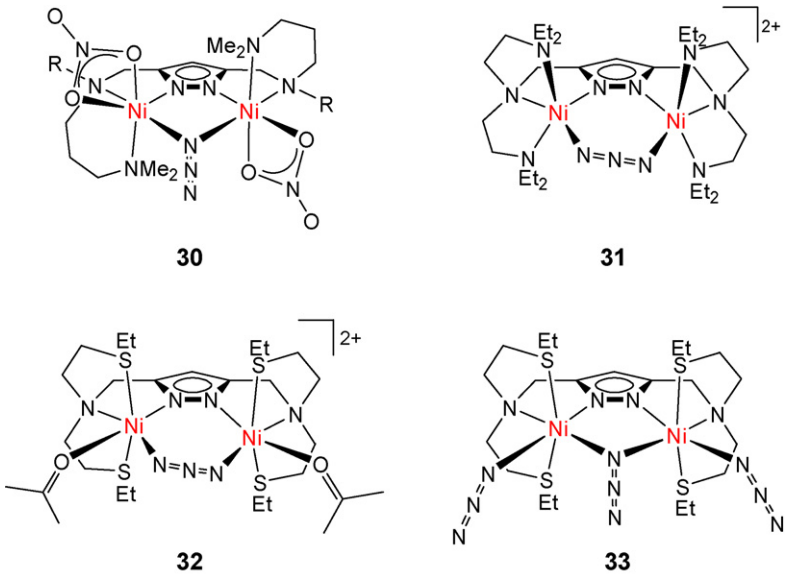

Scheme 12. Selection of pyrazolate-based nickel-azido complexes.

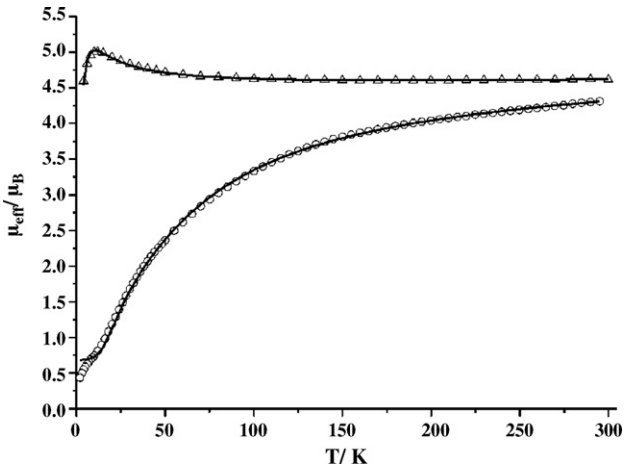

Fig. 19. Plot of μ_{eff} *versus T* for dinickel(II) complexes **30** (upper curve) and **31** (lower curve) [66]. The solid lines represent the calculated curve fits.

modes to be realized, depending on the solvent and conditions of crystallization (**32** and **34** *versus* **33**).

Of the two most common azide bridging modes, the μ-1,1 mode (*end-on*) usually entails ferromagnetic coupling, whereas the μ-1,3 (*end-to-end)* mode in most cases gives rise to antiferromagnetic behaviour [68]. A major problem in the rational design of metal/azide complexes is control over the azide binding mode, since it often is impossible to synthetically predict which bridging type will be adopted [12a]. Constraining the metal···metal separation by binucleating ligands provides a solution to this problem and thus determines the magnetic properties of the bimetallic entities (Fig. 19). While coupling between the two nickel(II) ions in **30** is ferromagnetic ($J = +4.0 \pm 0.5\,cm^{-1}$) to give an $S = 2$ ground state (neglecting zero-field splitting), it is antiferromagnetic with ground state $S = 0$ in **31** ($J = -25.7 \pm 0.3\,cm^{-1}$), as anticipated from the respective azide bridging modes [66].

The neutral dinickel complex **34** that contains a μ-1,3 azido bridge and two terminal azides shows very unusual magnetic properties with a pronounced step in the temperature dependence of μ_{eff} at around 215 K [69]. This could be attributed to a thermal phase transition due to a toggle-switch behaviour of the bridging azide: in the low temperature regime, the azide is found roughly within the plane defined by the pyrazolate and the two nickel ions

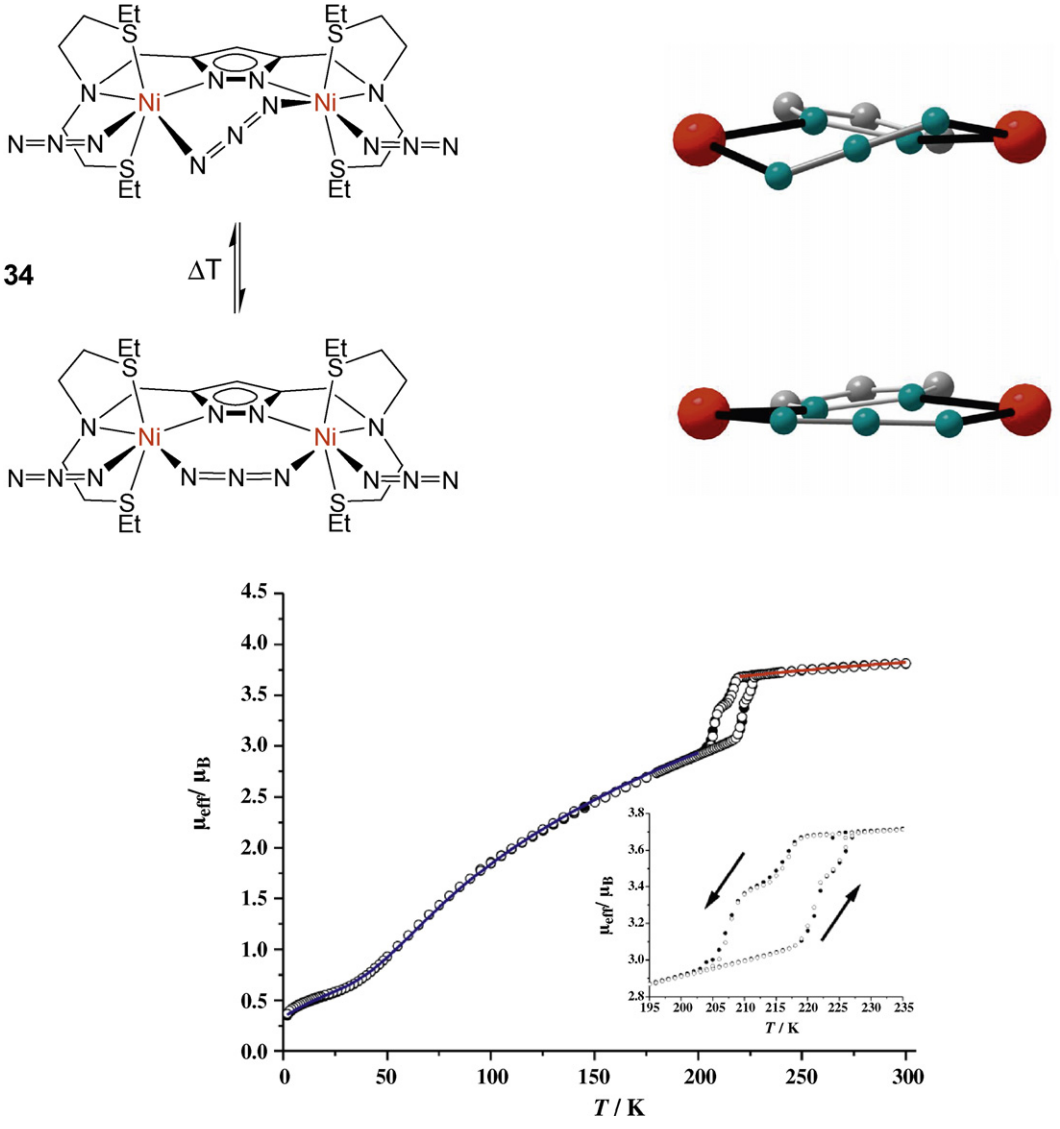

Fig. 20. Temperature-induced structural changes (top) and magnetic properties (bottom) of the μ-1,3 azido bridged dinickel(II) complex **34** [69].

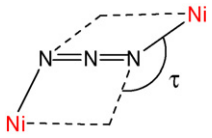

Scheme 13. Ni–NNN–Ni torsion τ.

(torsion angle Ni–NNN–Ni of 4.3°). At high temperatures, however, the azide bridge is severely tilted (torsion angle −46.6°). This transition occurs reversibly and with a rather wide hysteresis loop of $\Delta T \approx 13$ K, and single crystals of **34** stay intact upon repeated shuttling through the hysteresis range (X-ray data have been collected at different temperatures below and above the transition temperature). Since the magnetic coupling between μ-1,3 azido bridged metal ions depends on the Ni–NNN–Ni torsion τ (with strongest antiferromagnetic coupling when the two metals and the azide are in plane) [56], the azide in **34** essentially acts a switch that turns on or off the coupling (Fig. 20, Scheme 13).

Closer inspection of the crystallographic changes accompanying the phase transition have revealed that the sulphur bound ethyl groups of the ligand side arms in **34** are disordered about two positions at temperatures above the hysteresis range, whereas no disorder is present below the hysteresis range. Freezing of the disorder leads to a more efficient packing of the molecules at low temperatures and an abrupt shrinking of the crystallographic *a* axis upon cooling through the hysteresis regime, whereas changes of the *b* and *c* axes are only minor. It remains unclear, however, how the appearance or disappearance of disorder is coupled to the changes of the dihedral Ni–NNN–Ni angle within the bimetallic molecules, and whether the structural changes induce the changes in electronic/magnetic properties, or *vice versa*. The phase transition exhibits a two-step characteristics in some cases (Fig. 20), but this appears to be strongly dependent on crystal shape and subtle differences in crystallization conditions. This unusual phenomenon is still under active investigation.

Since materials that exhibit magnetic bistability near room temperature are expected to have great potential for future memory or sensing applications [70], the unusual hysteretic structural and magnetic properties of complex **34** have attracted some attention, and a detailed DFT analysis of the changes in μ_{eff} has meanwhile been carried out [71].

Dinickel complexes such as **32** and **34** serve as valuable building blocks for the targeted synthesis of one-dimensional (1D) linear-chain Heisenberg antiferromagnets (LCHAs) that inherently feature bond alternation (type **C**, Scheme 14). Such systems (HABAs), which otherwise have mostly been obtained by serendipity, may show interesting magnetic properties with gapless excitation at certain quantum critical points or a gapped ground state that is either in the singlet-dimer or in the Haldane phase. While these 1D systems are not the topic of the present review, it should be mentioned that the modular approach using pyrazolate-derived bimetallic building

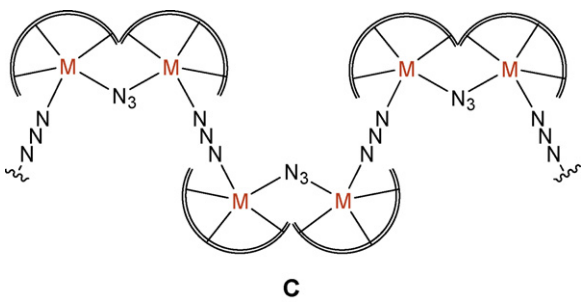

C

Scheme 14. 1D metal-azido systems from bimetallic components.

blocks allows for some control of the bond alternation parameter $\gamma = J_1/J_2$ that describes the differences in magnetic coupling within the binuclear components and between them. Spin correlation in the various 1D nickel-azido systems has been analyzed by Quantum Monte Carlo simulations, and assignment of the two different J_1 and J_2 values was based on comparison with the magnetic characteristics found for the bimetallic constituents. This again emphasizes the advantages of the modular building block approach [72,73].

4.2.2. Tetranuclear nickel(II) complexes

In an approach similar to the one described in Section 3.1, bimetallic complexes such as **30** that feature labile coligands in suitably oriented positions (the nitrate ions in **30**) can be used as building blocks for the assembly of tetranuclear complexes that readily form upon addition of additional azide bridges (Scheme 15) [66,74]. Different species **D** or **E** may form, depending on the metal/azide ratio, with the central azide ions in **E** adopting the rather uncommon triply bridging μ-1,1,3 mode.

The unique type **E** complex **35**, where the two dinickel(II) components are dislocated with respect to each other (Fig. 21), has an $S = 0$ ground state that can be analyzed by the proper spin Hamiltonian $\hat{H} = -2J_1(S_1S_3) - 2J_2(S_1S_2 + S_3S_4) - 2J_3(S_1S_4 + S_2S_3)$ to give $J_1 = -36.9\,cm^{-1}$, $J_2 = +18.9\,cm^{-1}$, $J_3 = +2.7\,cm^{-1}$, $g = 2.26$, $\rho = 1.0\%$, and TIP $= 6.5 \times 10^{-4}\,cm^3\,mol^{-1}$ [75,76]. Ferromagnetic coupling ($J_2 = +18.9\,cm^{-1}$) within the bimetallic constituents is reasonable because of the double μ-1,1 azide bridges, and antiferromagnetic coupling ($J_1 = -36.9\,cm^{-1}$) between the two central Ni ions is as expected for the double μ-1,3 azide linkage. Weakly ferromagnetic coupling for the paths denoted J_3 can be rationalized by the Ni–NNN–Ni torsion (109.3°) that is close to 90°, i.e., not far form an orthogonal situation. This suggests that magnetostructural correlations established for the common μ-1,1 and μ-1,3 modes also hold for the μ-1,1,3 azide bridges.

A series of rectangular type **D** Ni_4 complexes **36** (Fig. 22) could be obtained in crystalline form with R = Me or $(CH_2)_3NMe_2$ and different counteranions (ClO_4^-, BPh_4^-), and as different solvates (depending on the solvent of crystallization) [66,74]. Magnetic data have been analyzed according to the Hamiltonian

$$\hat{H} = -2J_1(\hat{S}_1\hat{S}_2 + \hat{S}_3\hat{S}_4) - 2J_2(\hat{S}_2\hat{S}_3 + \hat{S}_1\hat{S}_4) + \sum_{i=1}^{4}(D\hat{S}_{iz}^2 + g_i\mu_B B\hat{S}_{iz})$$

While *intra*subunit coupling within the dinickel(II) entities is always ferromagnetic as expected ($J_1 > 0$), the overall ground state of these Ni_4 systems may be either $S = 0$ or $S = 4$ (neglecting any zero-field splitting), depending on the Ni–NNN–Ni torsion for the linkages between the two subunits. When the torsion angle is close to 90°, an orthogonal orbital situation arises and the *inter*subunit coupling becomes ferromagnetic as well ($J_2 > 0$).

An interesting observation was made when studying the derivative [**36b**]$(BPh_4)_2 \cdot 2$acetone that was obtained from acetone/light petroleum solution [74]. A freshly prepared sample displays overall antiferromagnetic coupling, while data for a powdered sample that has been stored in air for prolonged times, or has briefly been kept under vacuum, shows ferromagnetic coupling (Fig. 23). IR spectra revealed that the band at $1707\,cm^{-1}$ for the fresh sample (that is characteristic for the C=O stretch of acetone included in the crystal lattice) has disappeared for the aged sample. This suggests a structural change of the Ni_4 core that is accompanied by a significant increase in Ni–NNN–Ni torsion upon extrusion of the acetone solvent molecules, leading to a drastic change in the magnetic properties. It was concluded that any magnetostructural correlation deduced from single crystal X-ray results and magnetic powder data should be treated with great caution, since subtle structural differences may easily exist between the powder and the crystal,

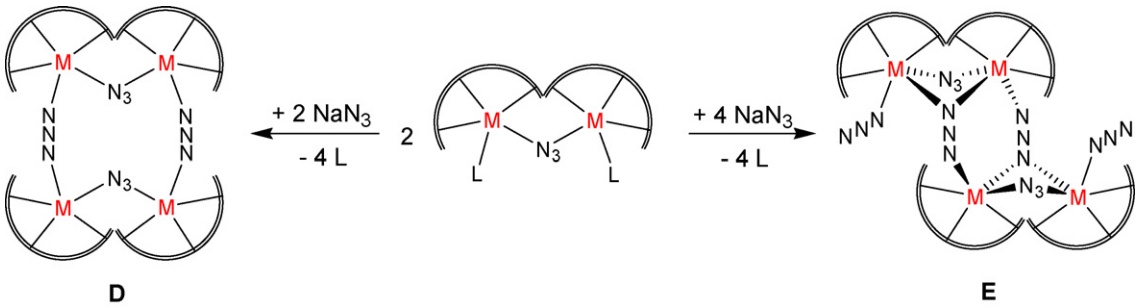

Scheme 15. Controlled assembly of tetranuclear species from bimetallic metal/azide building blocks.

but with substantial effects on the magnetic properties [74]. This is particularly true for systems with the flexible azido ligand, and if solvent is included in the crystal lattice.

Novel Ni_4 azido complexes of types **F**, **G**, and **H** (Scheme 16) with uncommon μ_3 and μ_4 azide binding modes have been obtained for the pyrazole ligands HL^{11R} and HL^{12} with appended thioether arms in the presence of carboxylates [77–79].

The central Ni_4 cores of type **F** complexes **37** consist of two $\{L^{11R}Ni_2\}$ fragments that are hold together by three azido ligands and a single carboxylate that spans the two subunits (Fig. 24). Two of the azido ligands adopt the rare μ_3-1,1,3 binding mode, while the third one links the two subunits as a μ-1,3 azide. Magnetic data reveal an overall $S_T = 0$ ground state and were analyzed according to the coupling scheme in Fig. 24, i.e., with the Hamiltonian

$$\hat{H} = -2J_1(\hat{S}_1\hat{S}_3) - 2J_2(\hat{S}_1\hat{S}_2 + \hat{S}_3\hat{S}_4) - 2J_3(\hat{S}_1\hat{S}_4 + \hat{S}_2\hat{S}_3) - 2J_4(\hat{S}_2\hat{S}_4) + \Sigma g\mu_B B\hat{S}_{iz}$$

The individual J values for the different exchange paths in complexes **37** confirm that magnetostructural correlations for the common μ-1,1 and μ-1,3 azide binding modes are also valid for the unusual μ-1,1,3 bridges. Coupling mediated by the double μ-1,1 azide linkage (J_1) is strongly ferromagnetic as expected, and coupling along the μ-1,3 linkage (J_4) is weakly ferromagnetic because of the close to orthogonal situation (torsion angle

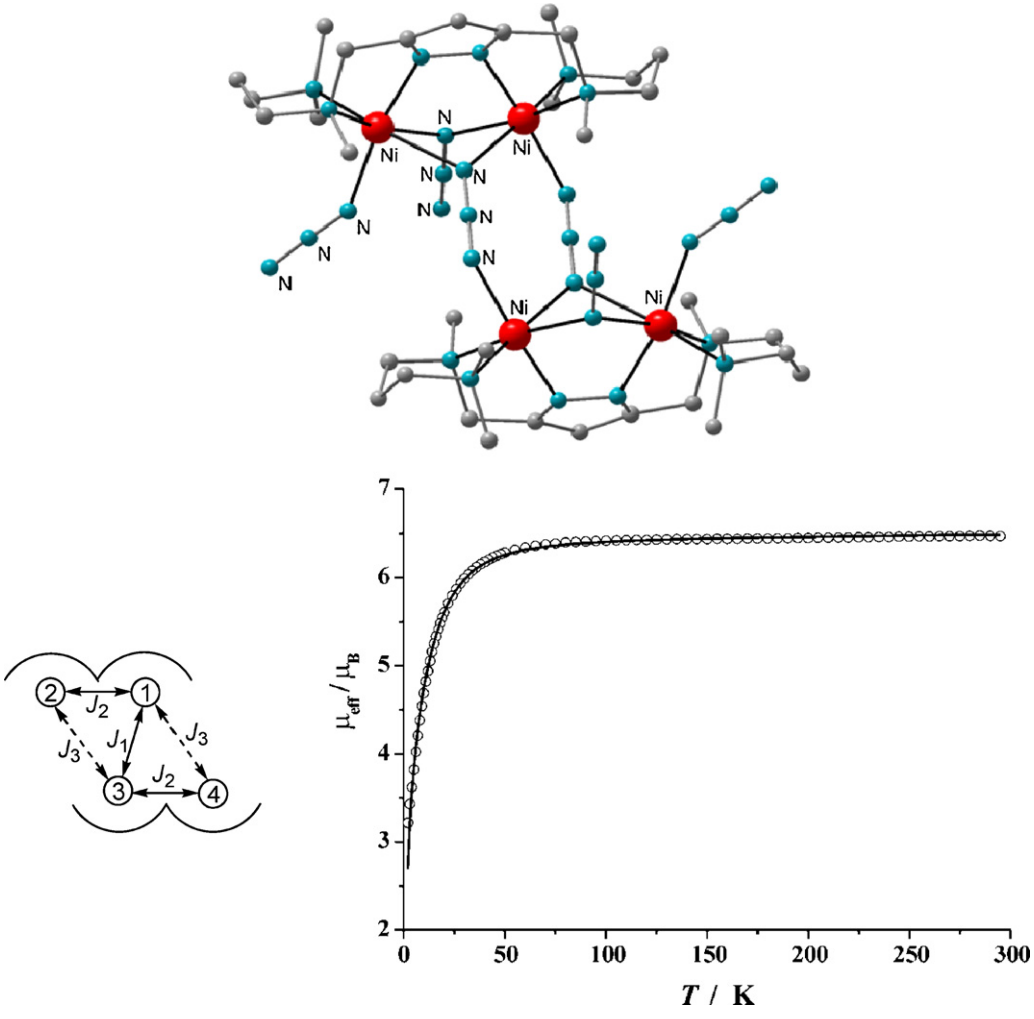

Fig. 21. Molecular structure of **35** (top) and its magnetic properties with appropriate coupling scheme (bottom).

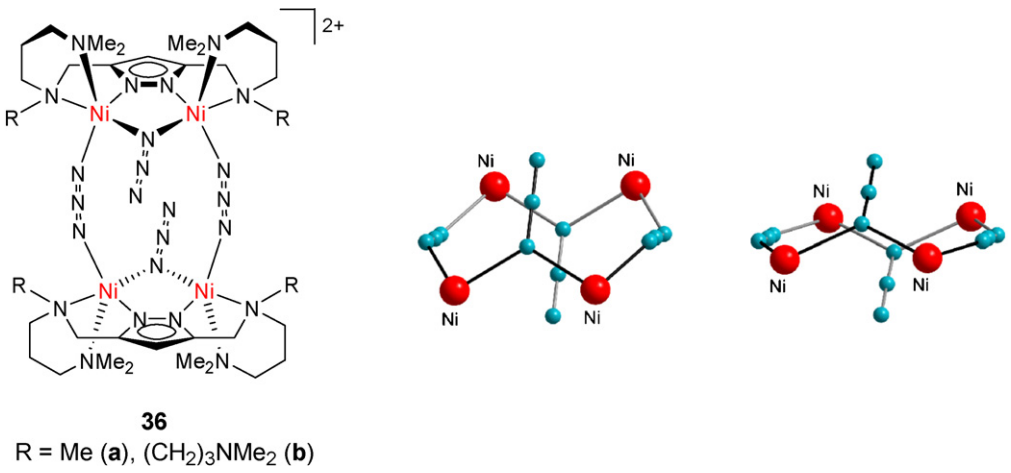

Fig. 22. Type **D** Ni_4 complexes **36** (left) and view of the central Ni_4 core for different examples in the solid state (right) with different Ni–NNN–Ni torsions [74].

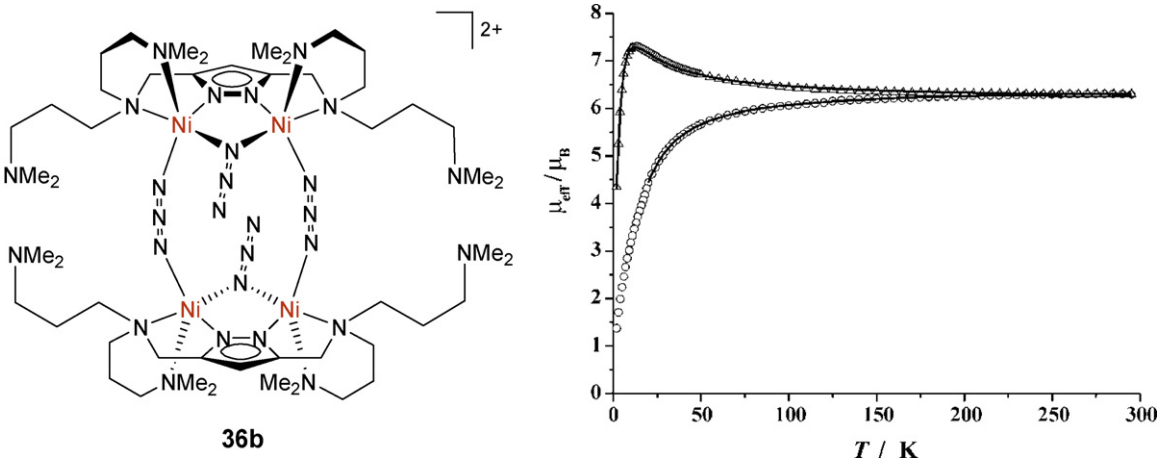

Fig. 23. Plot of μ_{eff} *versus* T for Ni_4-complex [**36b**]$(BPh_4)_2$ crystallized from acetone/ditheyl ether: fresh sample (upper curve) and after storage in air or applying vacuum (lower curve) [74].

Ni–NNN–Ni in the range 99–117° for the different compounds **37a–c**) and the relatively large Ni–N–N angles. Nickel ions within each pyrazolate-based bimetallic fragment are strongly antiferromagnetically coupled (J_2), while antiferromagnetic coupling is much weaker along the *inter*dimer μ-1,1,3 azide path (J_3) due to the Ni–NNN–Ni torsion [78].

Upon addition of a further equivalent of carboxylate, the Ni_4 core of type **F** complexes is opened up to give Ni_4 systems **H** with a more flattened topology and unprecedented μ-1,1,3,3 azido units [77]. The same complexes can also be obtained in a one-pot reaction starting from the proper stoichiometric amounts of the respective pyrazolate ligand, a nickel(II) salt, sodium azide, and the respective carboxylate. In the case of adamantyl carboxylate and with a different azide/carboxylate ratio, the related type **G** Ni_4 complexes are formed. Both type **G** and **H** systems feature the unusual central μ-1,1,3,3 azide, but with clearly different arrangements of the four nickel ions and with very different Ni–N–Ni angles and Ni–NNN–Ni torsions (**38** and **39** in Fig. 25) [79]. Apparently the μ-1,1,3,3 bridge is quite flexible and may adapt to different complex topologies.

All type **G** and **H** compounds have an $S_T = 0$ ground state, but J values for the individual *intra*dimer and *inter*dimer coupling paths differ significantly depending on the geometric details of the Ni_4 core, with the torsion along the central μ-1,1,3,3 playing a major role. In view of the novelty of this type of compounds with their unprecedented μ-1,1,3,3 azide, a more detailed study of a selected example has been undertaken.

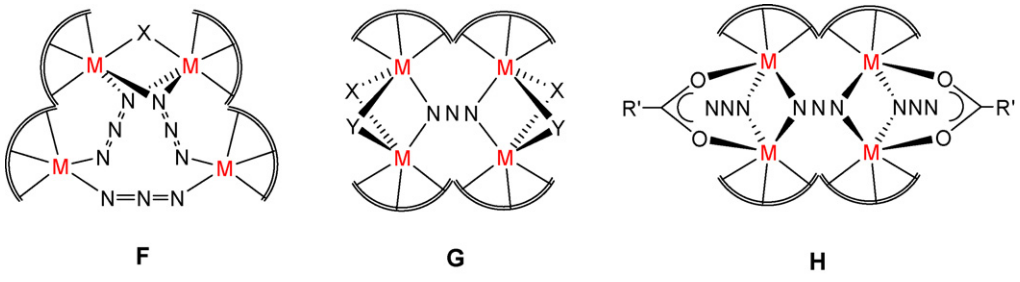

Scheme 16. Ni_4 azido complexes with uncommon μ_3 and μ_4 azide binding modes.

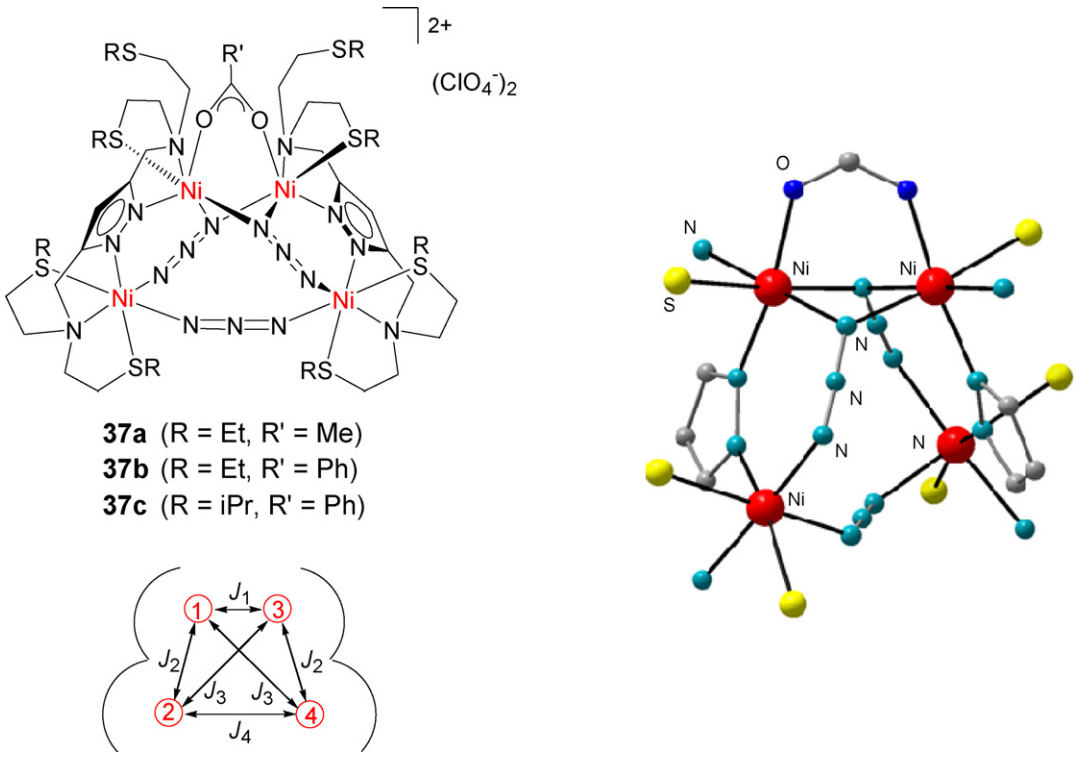

Fig. 24. Molecular structure of the Ni_4-complex **37a** and magnetic coupling scheme [78].

4.3. *High-frequency high-field EPR and pulsed-field magnetization*

High-frequency high-magnetic field EPR (HF-EPR) and static magnetization experiments have been performed on a selected example of the type **G** tetranuclear nickel(II) complexes with genuine μ_4-1,1,3,3 azide bridge. Most interestingly, complex **39** shows a transition from a nonmagnetic state to a magnetic one in magnetic fields stronger than a critical field of $H_{crit} \sim 25$ T (for details see Ref. [30,80]). All magnetic measurements have been performed on a powder sample pressed in a pellet with the experimental equipment described in Ref. [30].

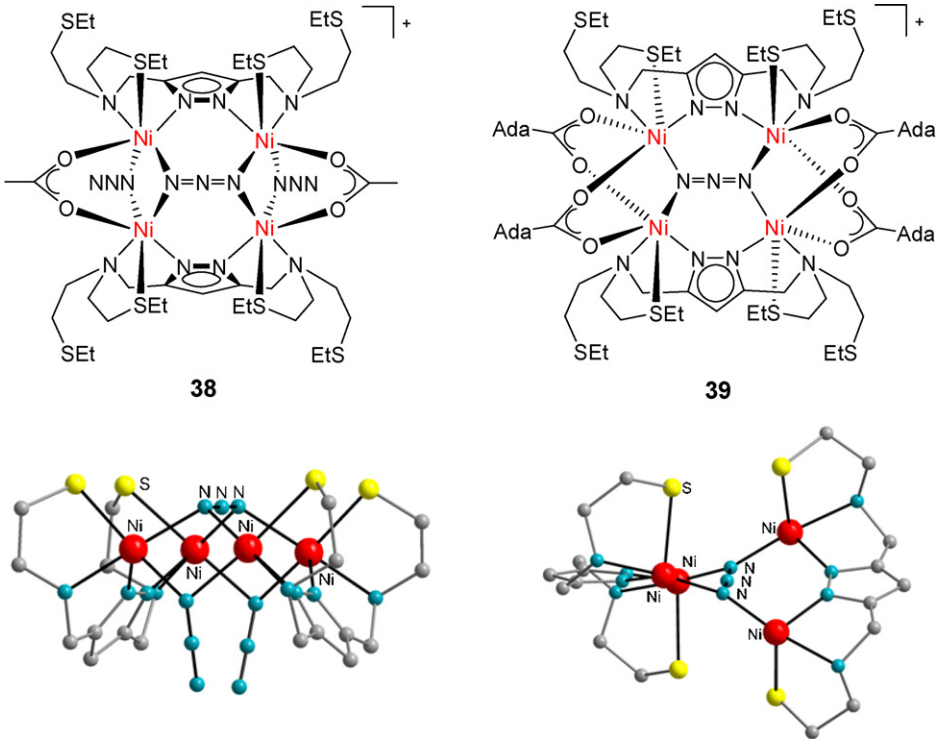

Fig. 25. Molecular structures of the Ni_4-complexes **38** and **39** [77,79].

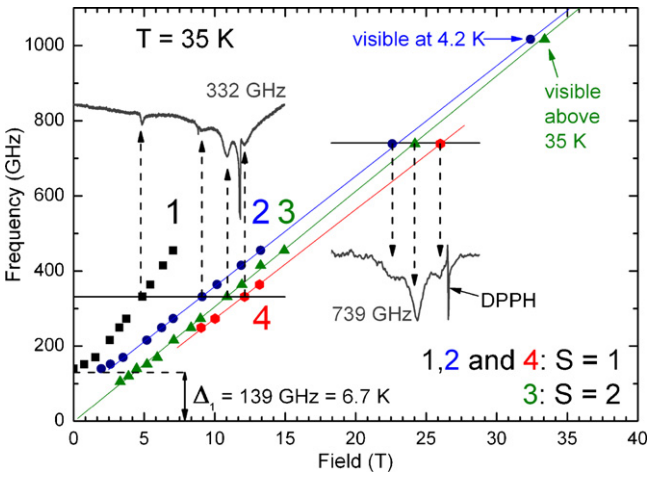

Fig. 26. Four resonance branches of the tetranuclear Ni(II) complex at $T = 35$ K and typical EPR spectra. Branches 1 and 2 exhibit a finite gap Δ_1. At $\nu = 1.017$ GHz resonance 2 is observed at 4.2 K owing to the spin level crossing (see the text).

HF-EPR was studied at frequencies $\nu = 0.1$–1 THz. The spectrum at elevated temperatures consists of four resonance modes $i = 1..4$ which at a constant value of ν occur at different resonance fields H_i^{res}. The respective ν *versus* H_i^{res} relations (resonance branches) together with the representative spectra are shown in Fig. 26.

Extrapolation of the $\nu(H_i^{res})$-dependences to zero field reveals a finite energy gap $\Delta_1 = 139$ GHz (6.7 K) for branches 1 and 2 and no gap for branches 3 and 4.

At $\nu < 1$ THz the intensities of the modes $I_i(T)$ follow a thermal activation behavior (Fig. 27a). Their sum $\Sigma_i I_i$ shows a T-dependence similar to the static susceptibility $\chi = M/H$ (Fig. 27b). This gives evidence that EPR probes the same Ni-spins which determine the static magnetic response. A strong decrease of $I_i(T)$ and $\chi(T)$ at low temperatures indicates a non-magnetic singlet ground state $S = 0$ of the $Ni(II)_4$-complex. Remarkably, resonances 1, 2 and 4 follow

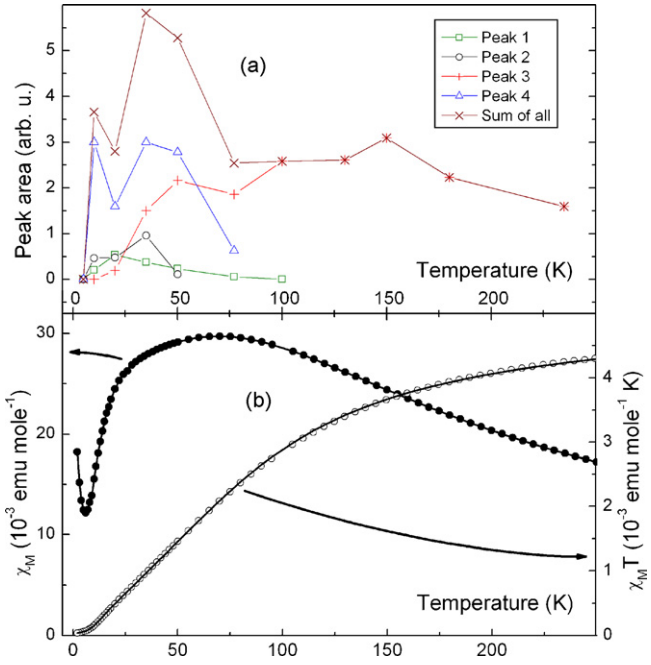

Fig. 27. (a) Temperature dependence of the intensities I_i of the resonance modes and of their sum ΣI_i. (b) static susceptibility $\chi = M/H$ and $\chi(T)T$ at a field of 0.5 T. A Curie-like tail below 20 K is due to ~2% of impurities. Solid lines are data fits (see the text).

a common temperature behavior with maxima at ~30 K, whereas resonance 3 has a broad maximum at ~150 K. One can assign therefore peaks 1, 2 and 4 to the first excited magnetic state $S = 1$ and peak 3 to the second excited state $S = 2$ of the complex. From the slopes of the $\nu(H_i^{res})$-dependences at high fields one can derive the g-factors. The values are typical for the Ni(II) ion and amount to 2.11, 2.18 and 2.08 for branches 2, 3 and 4 respectively. Note that a much stronger slope of branch 1 indicates that it results from a 'forbidden' spin-flip transition (see below).

An important new feature appears in the HF-EPR spectrum measured at $\nu = 1.017$ THz. A strong and broad absorption signal arises at fields $H > 25$ T. It can be associated with resonance 2 (Fig. 26). Noteworthy the signal is seen at a temperature of 4.2 K and vanishes above 10 K that allows to identify resonance 2 in the high-field regime with the ground state excitation. At still higher temperatures a thermally activated signal assigned to branch 3 develops in the spectrum (Fig. 26).

To analyze the experimental data we introduce a minimal effective spin Hamiltonian H_{spin} in the form

$$H_{spin} = J_1(\mathbf{S}_1\mathbf{S}_2 + \mathbf{S}_3\mathbf{S}_4) + J_2(\mathbf{S}_1\mathbf{S}_3 + \mathbf{S}_2\mathbf{S}_4) + J_3(\mathbf{S}_1\mathbf{S}_4 + \mathbf{S}_2\mathbf{S}_3) + D\sum_{i=1..4}[S_{iz}^2 - 1/3S_{Ni}(S_{Ni}+1)] + g\mu_B\mathbf{H}\sum_{i=1..4}\mathbf{S}_i.$$

Here, the first three terms represent the isotropic intramolecular magnetic coupling between the Ni spins $\mathbf{S}_i$ which assume three exchange paths described by the exchange couplings $J_{1,2,3}$ (Fig. 28). The fourth term describes the single-ion anisotropy D of the Ni(II) ions arising due to the influence of the anisotropic ligand crystal field (CF) and the spin–orbit coupling. This anisotropy yields a splitting of the spin states of a Ni ion in zero magnetic field (so-called zero field gap) whose magnitude is proportional to the anisotropy parameter D. The last term of H_{spin} is the Zeeman interaction with the external field $\mathbf{H}$. Here, g is the Ni(II) g-factor. In this model the much weaker intermolecular interactions are neglected.

Since in the powder HF-EPR spectrum the most spectral weight is caused by the microcrystallites having their CF anisotropy axis $\boldsymbol{c}$ close to the perpendicular direction to the magnetic field $\mathbf{H}$ it is appropriate to consider the energy spectrum of the spin states for the case $\boldsymbol{c}\perp\mathbf{H}$. Details of the combined analysis of the susceptibility $\chi(T)$ (Fig. 27) and EPR data (Fig. 26) in the framework of the above Hamiltonian H_{spin} can be found in Ref. [30]. Here we summarize the main results. The following hierarchy of the coupling parameters has been found: $J_1 = 37.3$ K (antiferromagnetic (AF) coupling), $J_2 = 57.8$ K (ferromagnetic (FM)) and a diagonal exchange $J_3 = 37.1$ K (AF). The respective coupling scheme is shown in Fig. 28 where pairs of FM coupled ions (1,3) and (2,4) interacting antiferromagnetically through J_1 and J_2 are depicted. The energy gap $\Delta_1 = 6.7$ K observed for branches 1 and 2 can be

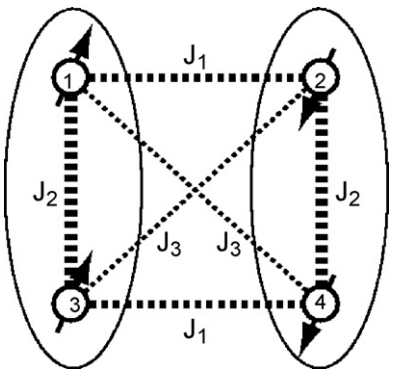

Fig. 28. Intramolecular magnetic couplings $J_{1,2,3}$ between the Ni spins $S_{Ni} = 1$ in **39**.

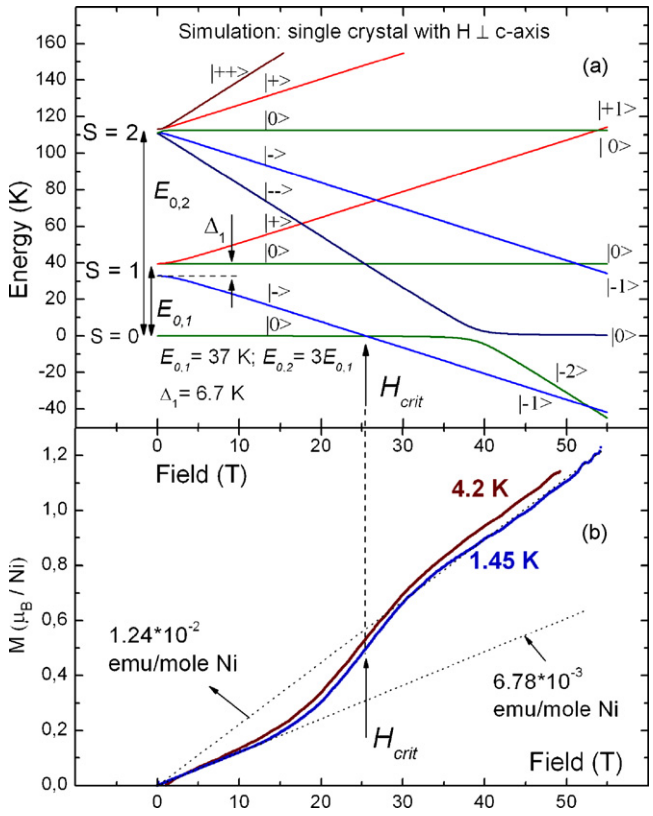

Fig. 29. (a) Energy diagram of the low lying spin levels of the tetranuclear Ni(II)-complex. Note the level crossing at $H_{crit} \sim 25$ T. (b) Field dependence of the magnetization $M(H)$ at $T = 1.45$ K and 4.2 K. Note a step-like increase of $M(H)$ around $H_{crit} \sim 25$ T. Dotted lines indicate a linear background at low- and high fields (see the text).

related to the Ni(II) single ion anisotropy yielding the anisotropy parameter $D = -0.72\ \Delta_1 = -4.8$ K. The numerical solution of the Hamiltonian H_{spin} with the above parameters yields the following three low-energy multiplets of the tetranuclear Ni(II)-complex: A nonmagnetic singlet ground state, $S = 0$, the first excited triplet state, $S = 1$, at the energy $E_{0,1} \approx 37$ K and the second excited quintuplet state, $S = 2$, at the energy $E_{0,2} \approx 3\ E_{0,1}$ (Fig. 29). The remaining $S = 3$ and $S = 4$ multiplets lie at even higher energies and are not considered for simplicity.

HF-EPR branches 1, 2 and 4 can be straightforwardly assigned to the excitations within the $S = 1$ multiplet. Branch 1 showing the zero field gap Δ_1 is a so-called 'forbidden' transition between levels labelled as $|-\rangle$ and $|+\rangle$ in Fig. 4a which in small magnetic fields are the mixture of $|-1\rangle$ ($S^z = -1$) and $|+1\rangle$ ($S^z = +1$) spin states of the $S = 1$ multiplet due to the CF effect and the spin–orbit coupling. Branch 2 showing the same gap is the transition between $|0\rangle$ and $|-\rangle$ states. The gapless branch 4 is the transition between $|0\rangle$ and $|+\rangle$ states. From the analysis of the temperature dependences of the HF-EPR peaks $I_i(T)$ (Fig. 27a) branch 3 has been ascribed to the transitions within the second excited $S = 2$ multiplet. Since the zero field splitting in this multiplet is almost absent (Fig. 29a) individual transitions $|--\rangle \leftrightarrow |-\rangle$, $|-\rangle \leftrightarrow |0\rangle$, $|0\rangle \leftrightarrow |+\rangle$ and $|+\rangle \leftrightarrow |++\rangle$ occur at practically the same resonance field and contribute therefore to the same line.

The calculated field dependence of the spin state energies suggests the change of the ground state to a magnetic one at $H > H_{crit} \sim 25$ T owing to the crossing of the $|-1\rangle$ level of the $S = 1$ multiplet with the $S = 0$ singlet at a critical field H_{crit} (Fig. 29a). The HF-EPR data at the excitation frequency $\nu = 1.017$ THz give strong experimental evidence for the spin level crossing. At this frequency the resonance field of peak 2 exceeds H_{crit}. Therefore the excitation from the $|-1\rangle$ to the $|0\rangle$ level becomes a ground state excitation which explains the observation of resonance 2 at a low temperature of 4.2 K (Fig. 26).

An additional confirmation of the spin level crossing comes from the low temperature magnetization $M(B)$ data (Fig. 29b). A broad step-like increase of the magnetization around 25 T clearly indicates the change of the ground state related to the level crossing at H_{crit}. Remarkably, one finds an appreciable increase of the magnetization M even at small fields $\mathbf{H} \ll H_{crit}$ which gets even stronger in the high field regime. Such additional contribution to M suggests a substantial admixture of the $S = 1$ multiplet to the ground state singlet $S = 0$ which may occur in the presence of the anisotropic Dzyaloshinsky–Moriya (DM) interaction, as has been theoretically modelled in Ref. [81].

4.4. Conclusions and perspectives

Pyrazolate-based binucleating ligands have been established as very valuable scaffolds in nickel/azido chemistry. By varying the chelate side arms of the central pyrazolate bridge, different metal···metal separations can be enforced, which in turn dictates the mode of azide binding. In the case of μ-1,3 azide bridges the Ni–NNN–Ni torsion has been identified as a crucial factor that determines the magnitude or even the sign of magnetic coupling (ferromagnetic or antiferromagnetic). Most interestingly, the μ-1,3 azide bridges have been shown to exhibit great flexibility, and the Ni–NNN–Ni may change with temperature or upon extrusion of lattice solvent from crystalline material. The reversible temperature-dependent azide tilting gives rise to fascinating hysteretic toggle-switch behaviour. On the other hand the changes that might occur upon drying of crystalline material demand caution when comparing magnetic data with information from single crystal X-ray crystallography.

The pyrazolate-derived bimetallic entities can be assembled in various ways, from tetranuclear species to alternating 1D chains systems. Depending on the ligand scaffold and the azide binding mode, either a diamagnetic ($S = 0$) or a high-spin ($S = 4$) magnetic ground state of the Ni_4 core can be obtained. Unusual μ_3-1,1,3 and novel μ_4-1,1,3,3 azide bridges supported by the pyrazolate-based Ni_4 platforms have been discovered, which complement the repertoire of azide binding modes in coordination chemistry (Scheme 17).

A selected example of a μ_4-1,1,3,3 azido-bridged Ni_4 complex has been studied in great detail by high-frequency high-field EPR and pulsed-field magnetization to reveal a transition from a nonmagnetic state to a magnetic one above a critical magnetic field of ~25 T. Analysis of the different coupling paths within the Ni_4 complex indicate that magnetostructural correlations known for

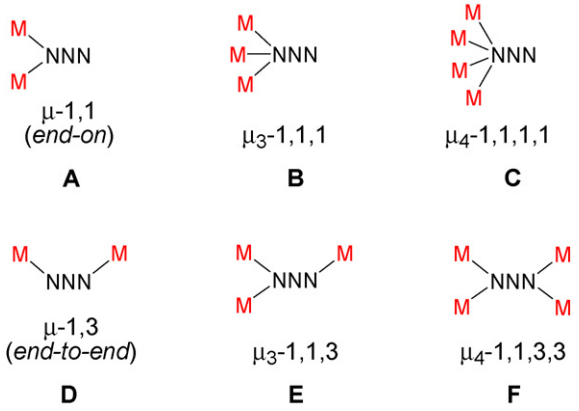

Scheme 17. Diversity of azide bridging.

the common μ-1,1 and μ-1,1 azide linkages also hold for the μ_3-1,1,3 and μ_4-1,1,3,3 bridges. This opens new perspectives for the use of azide as a bridging ligand and as magnetic coupler in high-nuclearity systems.

Acknowledgements

Generous funding by the Deutsche Forschungsgemeinschaft (SPP 1137) is gratefully acknowledged. P.C. also thanks the Max-Planck Society for continuous financial support. All authors wish to express their deepest gratitude to the colleagues and students whose names appear in the references for their enthusiasm and invaluable contributions. P.C. thankfully acknowledges skilful technical assistance of H. Schucht, R. Wagner, U. Pieper and A. Goebels.

References

[1] O. Kahn, Molecular Magnetism, VCH, New York, 1993.
[2] See for example;
R.E.P. Winpenny, Adv. Inorg. Chem. 52 (2001) 1.
[3] L. Thomas, F. Lionti, R. Ballou, D. Gatteschi, R. Sessoli, B. Barbara, Nature 383 (1996) 145.
[4] Review article:
D. Gatteschi, R. Sessoli, A. Cornia, Chem. Commun. (2000) 725.
[5] (a) D. Gatteschi, R. Sessoli, J. Villain, Molecular Nanomagnets, Oxford University Press, Oxford, 2006;
(b) J.R. Gispert, Coordination Chemistry, Wiley–VCH, Weinheim, 2008, pp. 295ff.
[6] (a) D. Gatteschi, R. Sessoli, Angew. Chem. 115 (2003) 278;
D. Gatteschi, R. Sessoli, Angew. Chem. Int. Ed. 42 (2003) 268;
(b) C.J. Milios, S. Piligkos, E.K. Brechin, Dalton Trans. (2008) 1809;
(c) E. Terazzi, C. Bourgogne, R. Welter, J.-L. Gallani, D. Guillon, G. Rogez, Angew. Chem. 120 (2008) 500;
E. Terazzi, C. Bourgogne, R. Welter, J.-L. Gallani, D. Guillon, G. Rogez, Angew. Chem. Int. Ed. 47 (2008) 490;
(d) C.J. Milios, A. Vinslava, W. Wernsdorfer, S. Moggach, S. Parsons, S.P. Perlepes, G. Christou, E.K. Brechin, J. Am. Chem. Soc. 129 (2007) 2754;
(e) A. Cornia, A.F. Costantino, L. Zobbi, A. Caneschi, D. Gatteschi, M. Mannini, R. Sessoli, Struct. Bond 122 (2006) 133.
[7] M. Cavallini, M. Facchini, C. Albonetti, F. Biscarini, Phys. Chem. Chem. Phys. 10 (2008) 784.
[8] M. Cavallini, J. Gomez-Segura, D. Ruiz-Molina, M. Massi, C. Albonetti, C. Rovira, J. Veciana, F. Biscarini, Angew. Chem. 117 (2005) 910;
M. Cavallini, J. Gomez-Segura, D. Ruiz-Molina, M. Massi, C. Albonetti, C. Rovira, J. Veciana, F. Biscarini, Angew. Chem. Int. Ed. 44 (2005) 888.
[9] M.N. Leuenberger, D. Loss, Nature 410 (2001) 789.
[10] E. Coronado, J.R. Galán-Mascarós, C.J. Gómez-García, V. Laukhin, Nature 408 (2000) 447.
[11] J.A. Rikken, E. Raupach, Nature 390 (1997) 493.
[12] (a) J. Ribas, A. Escuer, M. Monfort, R. Vicente, R. Cortés, L. Lezama, T. Rojo, Coord. Chem. Rev. 193–195 (1999) 1027;
(b) H.O. Stumpf, Y. Pei, O. Kahn, J. Sletten, J.P. Renard, J. Am. Chem. Soc. 115 (1993) 6738;
(c) E. Coronado, J.R. Galán-Mascarós, C.J. Gómez-García, J.M. Martínez-Agudo, Inorg. Chem. 40 (2001) 113;
(d) M. Ohba, H. Okawa, Coord. Chem. Rev. 198 (2000) 313;
(e) K.J. Nelson, I.D. Giles, S.A. Troff, A.M. Arif, J.S. Miller, Inorg. Chem. 45 (2006) 8922.
[13] (a) A. Caneschi, D. Gatteschi, R. Sessoli, P. Rey, Acc. Chem. Res. 22 (1989) 392;
(b) C. Benelli, D. Gatteschi, Chem. Rev. 102 (2002) 2369;
(c) J.S. Miller, Dalton Trans. (2006) 2742;
(d) J.-N. Rebilly, T. Mallah, Struct. Bond. 122 (2006) 103;
(e) G. Aromí, E.K. Brechin, Struct. Bond. 122 (2006) 1;
(f) R. Jain, K. Kabir, J.B. Gilroy, K.A.R. Mitchell, K.C. Wong, R.G. Hicks, Nature 445 (2007) 291.
[14] J.M. Lehn, Supramolecular Chemistry: Concepts and Perspectives, VCH, Weinheim, 1995.
[15] A. Müller, F. Peters, M.T. Pope, D. Gatteschi, Chem. Rev. 98 (1998) 239.
[16] R.W. Saalfrank, B. Demleitner, in: J.P. Sauvage (Ed.), Perspective in Supramolecular Chemistry, vol. 5, Wiley–VCH, Weinheim, 1999.
[17] A.L. Dearden, S. Parsons, R.E.P. Winpenny, Angew. Chem. 113 (2001) 155;
A.L. Dearden, S. Parsons, R.E.P. Winpenny, Angew. Chem. Int. Ed. 40 (2001) 151.
[18] S.P. Watton, P. Fuhrmann, L.E. Pence, A. Caneschi, A. Cornia, G.L. Abbati, S.J. Lippard, Angew. Chem. 109 (1997) 2917;
S.P. Watton, P. Fuhrmann, L.E. Pence, A. Caneschi, A. Cornia, G.L. Abbati, S.J. Lippard, Angew. Chem. Int. Ed. Engl. 36 (1997) 2774.
[19] Selected examples:
(a) S.J. Gruber, C.M. Harris, E. Sinn, J. Inorg. Nucl. Chem. 30 (1968) 1805;
(b) R.L. Linkvedt, L.S. Kramer, G. Ranger, P.W. Corfield, M.D. Glick, Inorg. Chem. 22 (1983) 3580;
(c) C.B. Singh, B. Sahoo, J. Inorg. Nucl. Chem. 36 (1974) 1259;
(d) D. Luneau, H. Oshio, H. Okawa, S. Kida, J. Chem. Soc., Dalton Trans. (1990) 2283;
(e) Y. Pei, Y. Journaux, O. Kahn, Inorg. Chem. 27 (1988) 399;
(f) F. Lloret, Y. Journaux, M. Julve, Inorg. Chem. 29 (1990) 3967;
(g) P. Chaudhuri, M. Winter, P. Fleischhauer, W. Haase, U. Flörke, H.-J. Haupt, J. Chem. Soc., Chem. Commun. (1990) 1728.
[20] (a) P. Chaudhuri, Coord. Chem. Rev. 343 (2003) 143;
(b) P. Chaudhuri, Proc. Indian Acad. Sci. 111 (1999) 397.
[21] (a) C. Krebs, M. Winter, T. Weyhermüller, E. Bill, K. Wieghardt, P. Chaudhuri, J Chem. Soc., Chem. Commun. (1995) 1913;
(b) C.N. Verani, T. Weyhermüller, E. Bill, P. Chaudhuri, Chem. Commun. (1998) 2475.
[22] S. Khanra, T. Weyhermüller, E. Bill, P. Chaudhuri, Inorg. Chem. 45 (2006) 5911.
[23] P. Chakravorty, S.K. Chandra, Polyhedron 13 (1994) 683.
[24] P. Chaudhuri, T. Weyhermüller, unpublished results.
[25] Selected examples:
(a) D.R. Boston, N.J. Rose, J. Am. Chem. Soc. 90 (1968) 6859;
(b) J.E. Parks, B.E. Wagner, R.H. Holm, J. Am. Chem. Soc. 92 (1970) 3500;
(c) G.A. Zakrzewski, C.A. Ghilardi, E.C. Lingafelter, J. Am. Chem. Soc. 93 (1971) 4411;
(d) R.F. See, M.R. Churchill, K.A. Lance, D.P. Mersman, K.R. Williams, Inorg. Chim. Acta 257 (1997) 285;
(e) Y.Z. Voloshin, O.A. Varzatskii, T.E. Kron, V.K. Belsky, V.E. Zavodnik, N.G. Strizhakova, A.V. Palchik, Inorg. Chem. 39 (2000) 1907;
(f) S. Kubow, K.J. Takeuchi, J.J. Grzybowski, A.J. Tircitano, V.L. Goedken, Inorg. Chim. Acta 241 (1996) 21;
(g) C. Engrakul, W.J. Shoemaker, J.J. Grzybowski, I. Guzei, A. Rheingold, Inorg. Chem. 39 (2000) 5161.
[26] S. Jurisson, L. Francesconi, K.E. Linder, E. Treher, M.F. Malley, J.Z. Gougoutas, A.D. Nunn, Inorg. Chem. 30 (1991) 1820.
[27] E. Bill, Program "Julx", Max-Planck-Institut für Bioanorganische Chemie, Mülheim an der Ruhr, Germany, 2005.
[28] J. Zuo, J. Dou, D. Li, D. Wang, Y. Sun, Acta Cryst. E 63 (2007) m3183.
[29] (a) S. Khanra, B. Biswas, C. Golze, B. Büchner, V. Kataev, T. Weyhermüller, P. Chaudhuri, Dalton Trans. (2007) 481;
(b) P. Chaudhuri, T. Weyhermüller, R. Wagner, S. Khanra, B. Biswas, E. Bothe, E. Bill, Inorg. Chem. 46 (2007) 9003;
(c) T. Weyhermüller, R. Wagner, S. Khanra, P. Chaudhuri, DaltonTrans. (2005) 2539;
(d) S. Khanra, T. Weyhermüller, E. Rentschler, P. Chaudhuri, Inorg. Chem. 44 (2005) 8176;
(e) T.C. Stamatatos, E. Katsoulakou, A. Terzis, C.P. Raptopoulou, R.E.P. Winpenny, S.P. Perlepes, Polyhedron, 2008, doi:10.1016/j.poly.2008.10.040.;
(f) see for examples of other star-shaped molecules: R.W. Saalfrank, A. Scheurer, I. Bernt, F.W. Heinemann, A.V. Postinikov, V. Schünemann, A.X. Trautwein, M. Alam, H. Rupp, P. Müller, Dalton Trans. (2006) 2865 and references therein.
[30] C. Golze, A. Alfonsov, R. Klingeler, B. Büchner, V. Kataev, C. Mennerich, H.-H. Klauss, M. Goiran, J.-M. Broto, H. Rakoto, S. Demeshko, G. Leibeling, F. Meyer, Phys. Rev. B 73 (2006) 224403.
[31] J.R. Pilbrow, Transition Ion Electron Paramagnetic Resonance, Clrendon Press, Oxford, 1990;
(b) F.E. Mabbs, D. Collison, Electron Paramagnetic Resonance of d Transition Metal Complexes, Elsevier, Amsterdam, 1992.
[32] S. Ross, T. Weyhermüller, E. Bill, K. Wieghardt, P. Chaudhuri, Inorg. Chem. 40 (2001) 6656.
[33] B. Kersting, Eur. J. Inorg. Chem. (1998) 1071.
[34] B. Kersting, M.J. Kolm, C. Janiak, Z. Anorg. Allg. Chem. 624 (1998) 775.
[35] B. Kersting, G. Steinfeld, J. Hausmann, Eur. J. Inorg. Chem. (1999) 179.
[36] B. Kersting, Eur. J. Inorg. Chem. (1999) 2157.
[37] B. Kersting, D. Siebert, D. Volkmer, M.J. Kolm, C. Janiak, Inorg. Chem. 38 (1999) 3871.
[38] (a) B. Kersting, G. Steinfeld, Chem. Commun. (2001) 1376;
(b) M.H. Klingele, G. Steinfeld, B. Kersting, Z. Naturforsch. 56b (2001) 901.
[39] S. Brooker, Coord. Chem. Rev. 222 (2001) 33.
[40] A.C. Marr, D.J.E. Spencer, M. Schröder, Coord. Chem. Rev. 219–221 (2001) 1055.
[41] P.A. Vigato, S. Tamburini, L. Bertolo, Coord. Chem. Rev. 251 (2007) 1311.
[42] C. Loose, V. Lozan, J. Kortus, B. Kersting, Coord. Chem. Rev., in press, doi:10.1016/j.ccr.2008.08.016.
[43] M.H. Klingele, B. Kersting, Z. Naturforsch. 56b (2001) 437.
[44] B. Kersting, D. Siebert, Eur. J. Inorg. Chem. (1999) 189.
[45] B. Kersting, Z. Naturforsch. 53b (1998) 1379.
[46] B. Kersting, G. Steinfeld, T. Fritz, J. Hausmann, Eur. J. Inorg. Chem. (1999) 2167.
[47] R. Schenker, H. Weihe, H.U. Güdel, B. Kersting, Inorg. Chem. 40 (2001) 3355.
[48] B. Kersting, D. Siebert, Inorg. Chem. 37 (1998) 3820.
[49] G. Steinfeld, B. Kersting, Chem. Comm. (2000) 205.
[50] G. Siedle, B. Kersting, Z. Anorg. Allg. Chem. 632 (2006) 763.
[51] B. Kersting, G. Steinfeld, D. Siebert, Chem. Eur. J. 7 (2001) 4253.
[52] The magnetic properties of compound **9**$(BPh_4)_2$ have been communicated in preliminary form (see footnote 63 in Ref. [37]), but have not yet been published in detail.
[53] T. Glaser, T. Beissel, E. Bill, T. Weyhermüller, V. Schünemann, W. Meyer-Klaucke, A.X. Trautwein, K. Wieghardt, J. Am. Chem. Soc. 121 (1999) 2193.
[54] T. Beissel, T. Glaser, F. Kesting, K. Wieghardt, B. Nuber, Inorg. Chem. 35 (1996) 3936.
[55] Notice that D represents an effective zero-field splitting parameter, since the zero-field splitting tensors of all ions are assumed to be collinear. It

is also important to note that analysis of temperature dependent magnetic suscpetibility measurement are not very appropriate for the determination of the sign and magnitude of D. Thus, the D value of $-0.068\,cm^{-1}$ determined for **25** by magnetic susceptibility measurements should be taken as indicative rather than definitive. The D value of $-0.21\,cm^{-1}$ determined by HF-EPR spectroscopic measurements outlined below in 3.2 much more accurate.

[56] (a) A. Escuer, R. Vicente, J. Ribas, M.S. El Fallah, X. Solans, M. Font-Bardia, Inorg. Chem. 32 (1993) 3727;
(b) A. Escuer, R. Vicente, M.S. El Fallah, J. Ribas, X. Solans, M. Font-Bardía, J. Chem. Soc., Dalton Trans. (1993) 2975;
(c) A. Escuer, R. Vicente, J. Ribas, M.S. El Fallah, X. Solans, M. Font-Bardía, Inorg. Chem. 33 (1994) 1842;
(d) R. Vicente, A. Escuer, J. Ribas, M.S. El Fallah, X. Solans, M. Font-Bardía, Inorg. Chem. 34 (1995) 1278;
(e) J. Ribas, M. Montfort, B.K. Ghosh, R. Cortés, X. Solans, M. Font-Bardía, Inorg. Chem. 35 (1996) 864.

[57] Details of the pulsed field magnetization study will be published elsewhere. See also, C. Golze, PhD Thesis, Technical University of Dresden, 2007.

[58] A. Abragam, B. Bleaney, Electron Paramagnetic Resonance of Transition Ions, Oxford University Press, London, 1970.

[59] A. Bencini, D. Gatteschi, EPR of Exchange Coupled Systems, Springer, 1990.

[60] Details of the HF-EPR analysis will be published elsewhere. See also, C. Golze, PhD Thesis, Technical University of Dresden, 2007.

[61] M. Andruh, Chem. Commun. (2007) 2565.

[62] J. Klingele, S. Dechert, F. Meyer, Coord. Chem. Rev., in press, doi:10.1016/j.ccr.2009.03.026.

[63] See for example;
(a) F. Meyer, K. Heinze, B. Nuber, L. Zsolnai, J. Chem. Soc., Dalton Trans. (1998) 207;
(b) M. Konrad, F. Meyer, K. Heinze, L. Zsolnai, J. Chem. Soc., Dalton Trans. (1998) 199;
(c) J. Ackermann, F. Meyer, E. Kaifer, H. Pritzkow, Chem. Eur. J. 8 (2002) 247;
(d) J. Ackermann, F. Meyer, H. Pritzkow, Inorg. Chim. Acta 357 (2004) 3703.

[64] T.G. Schenck, J.M. Downes, C.R.C. Milne, P.B. Mackenzie, H. Boucher, J. Whelan, B. Bosnich, Inorg. Chem. 24 (1985) 2334.

[65] J.C. Röder, F. Meyer, H. Pritzkow, Organometallics 20 (2001) 811.

[66] G. Leibeling, S. Demeshko, B. Bauer-Siebenlist, F. Meyer, H. Pritzkow, Eur. J. Inorg. Chem. (2004) 2413.

[67] F. Meyer, S. Beyreuther, K. Heinze, L. Zsolnai, Chem. Ber./Recueil 130 (1997) 605.

[68] (a) M.-F. Charlot, O. Kahn, M. Chaillet, C. Larrieu, J. Am. Chem. Soc. 108 (1986) 2574;
(b) L.K. Thompson, S.S. Tandon, Comments Inorg. Chem. 18 (1996) 125;
(c) A. Escuer, G. Aromí, Eur. J. Inorg. Chem. (2006) 4721.

[69] G. Leibeling, S. Demeshko, S. Dechert, F. Meyer, Angew. Chem. 117 (2005) 7273;
G. Leibeling, S. Demeshko, S. Dechert, F. Meyer, Angew. Chem. Int. Ed. 44 (2005) 7111.

[70] O. Kahn, J.P. Launay, Chemtronics 3 (1988) 140.

[71] J. Bian, Y. Chang, J. Zhang, J. Phys. Chem. A 112 (2008) 3186.

[72] (a) F. Meyer, H. Pritzkow, Inorg. Chem. Commun. 4 (2001) 305;
(b) F.-M. Nie, S. Demeshko, S. Fuchs, S. Dechert, T. Pruschke, F. Meyer, Dalton Trans. (2008) 3971.

[73] S. Demeshko, G. Leibeling, S. Dechert, S. Fuchs, T. Pruschke, F. Meyer, ChemPhysChem 8 (2007) 405.

[74] S. Demeshko, G. Leibeling, S. Dechert, F. Meyer, Dalton Trans. (2006) 3458.

[75] Temperature-independent paramagnetism (TIP) and a Curie-behaved paramagnetic impurity (ρ) with spin $S=1$ were included according to $\chi_{calc} = (1-\rho)\chi + \rho\chi_{mono} + TIP$.

[76] An earlier analysis for **35** assuming $J_3 = 0$ gave $J_1 = -19.7\,cm^{-1}$, $J_2 = +6.0\,cm^{-1}$, $g = 2.29 \pm 0.02$, $\rho = 3.0\%$, and $TIP = 3.6 \times 10^{-4}\,cm^3\,mol^{-1}$ [66].

[77] F. Meyer, P. Kircher, H. Pritzkow, Chem. Commun. (2003) 774.

[78] F. Meyer, S. Demeshko, G. Leibeling, B. Kersting, E. Kaifer, H. Pritzkow, Chem. Eur. J. 11 (2005) 1518.

[79] S. Demeshko, G. Leibeling, W. Maringgele, F. Meyer, C. Mennerich, H.-H. Klauss, H. Pritzkow, Inorg. Chem. 44 (2005) 519.

[80] V. Kataev, C. Golze, A. Alfonsov, R. Klingeler, B. Büchner, M. Goiran, J.-M. Broto, H. Rakoto, C. Mennerich, H.-H. Klauss, S. Demeshko, G. Leibeling, F. Meyer, J. Phys.: Conf. Ser. 51 (2006) 351.

[81] N.P. Konstantinidis, D. Coffey, Phys. Rev. B 66 (2002) 174426/1.